12-2022

A Method for Exploring the Habitability of Earth-Like Exoplanets: Applications to TESS Objects of Interest 203 b, 256 b, and 700 d

Paul Bonney
University of Arkansas, Fayetteville

A Method for Exploring the Habitability of Earth-Like Exoplanets: Applications to TESS Objects of Interest 203 b, 256 b, and 700 d

A dissertation submitted in partial fulfillment
of the requirements for the degree of
Doctor of Philosophy in Physics

by

Paul Bonney
Millsaps College
Bachelor of Science in Mathematics, 2016

December 2022
University of Arkansas

This dissertation is approved for recommendation to the Graduate Council

Julia Kennefick, PhD
Dissertation Director

Pradeep Kumar, PhD
Committee member

Yong Wang, PhD
Committee member

Surendra Singh, PhD
Committee member

ABSTRACT

The Transiting Exoplanet Survey Satellite (TESS) has and is continuing to discover a multitude of potentially habitable planet candidates. As more planets are detected and confirmed, it becomes increasingly important to strategically search for signs of habitability with which to differentiate and prioritize them for further observation, in particular with the James Webb Space Telescope (JWST). To facilitate this, I have created a method for prioritizing TESS planet candidates based on parameters derived from their light curves and have applied the method to the TESS Candidate Target List (CTL). This data set uses preliminary fits to transit modeling which can rely on erroneous assumptions about the system, such as the use of a sun-like star to fit TESS Object of Interest (TOI) 700 d (Gilbert et al., 2020; Rodriguez et al. 2020). Such systems require additional followup fitting with proper inputs which is done after the initial prioritization. Nevertheless, this method identified two high-priority TOIs that lacked the extensive habitability study in this work: 256 and 203. I have further created a new modeling procedure and applied it to these TOIs as well as TOI 700 with the aim to constrain the possibility of liquid water being present. In most of the recent cases of observations targeting exoplanets, 3D General Circulation Models (GCMs) are used to infer planet composition and structure or to predict observations of scientific interest. However, previous modeling has focused on parameter spaces that are not statistically linked to the observational data (e.g. Del Genio et al. 2019a, Turbet et al. 2016). Accurate statistical modeling is vital to the confirmation of other habitable worlds. To address the problem, I have created a method to statistically investigate the habitability of exoplanets with a suite of 1D and 3D models using the *VPlanet* software package (Barnes et al. 2020) and

the ROCKE-3D GCM (Way et al. 2017). Furthermore, I have applied this method to the two TESS-observed planets and candidates which were most highly prioritized as well as TOI 700 d. This constitutes an end-to-end investigation of real TESS exoplanets and the potential for liquid water on their surfaces. This provides guidance for current and future NASA missions like JWST, helping to answer the question: is there life beyond Earth?

ACKNOWLEDGEMENTS

Thank you to my advisor, Dr. Julia Kennefick for mentoring me and keeping me on track. Thank you to my family for their constant support and love. Finally, and most importantly, thank you to my beloved partner, Tristan Bland, who inspired me to study this field.

TABLE OF CONTENTS

LIST OF FIGURES

LIST OF TABLES

1 Introduction

Finding life beyond our planet tantalizes the imaginations of people across the globe. Many attempts to accomplish this goal have been made throughout the years. Most famously, the Search for Extra-Terrestrial Intelligence (SETI) has studied the skies for potential signals from other civilizations among the stars.

Though we currently have no confirmation of extraterrestrial life, the search continues in and out of our solar system. Rovers currently scour the surface of Mars looking for the remnants of bacteria and a planned mission to Saturn's moon Titan is scheduled to launch in a few short years to examine pre-biotic chemical processes.

Since the first exoplanet was confirmed in 1995 (Mayor & Queloz, 1995), astronomers have attempted to reach beyond our solar system to find life on other worlds. Over a quarter century later, the James Webb Space Telescope (JWST) has launched to carry on this legacy of examining extrasolar planets for spectral signals that could carry the markers of life.

The validity of biomarkers, as these signals are called, is an active area of investigation. One facet of this debate is the definition of life itself: what can a living thing be? The presence of liquid water is a common requirement for life as we know it and the search for confirmation of liquid water on the surface of an exoplanet is a major goal of exoplanet astronomers.

While one day in the far future we may be able to set foot on an alien world, we must currently rely on the spectral "fingerprints" of a planet's atmosphere as the light from its host passes through it. This data, combined with complex climate modeling, may one day confirm the existence of liquid water on the surface of a terrestrial world. In the mean time,

the improvement of both detection and predictive modeling techniques is paramount for the field.

1.1 Exoplanet Detection

Exoplanets are detected in a variety of ways (Figure 1.1), though currently the most numerous detections are by the transit method (Figure 1.2). Transit photometry uses the temporary decrease in light as a planet transits its host star's face as we see it. For Earth-sized planets, the large ratio of star size to planet size makes this dip very small which requires sophisticated fitting procedures to analyze for the planet's characteristics such as radius and orbital period.

The paragon instruments of this method are the Kepler Space Telescope and Transiting Exoplanet Survey Satellite (TESS). Together, these missions have confirmed over 3000 exoplanets with thousands more awaiting confirmation.

It is important to note that planets solely detected through transit methods cannot have their mass measured. This parameter is extremely important in habitability modeling and is usually detected through the radial velocity method (Figure 1.3). In this method, the star's motion around the system's barycenter causes small amounts of Doppler shift in its spectrum. Analyzing this data while knowing the star's mass yields the mass of the planet with a dependence on $sin(i)$ or the sin of the inclination angle of the system. For transiting systems, the inclination angle is constrained to $\sim 90^{\circ}$ giving more accurate limitations on planet mass.

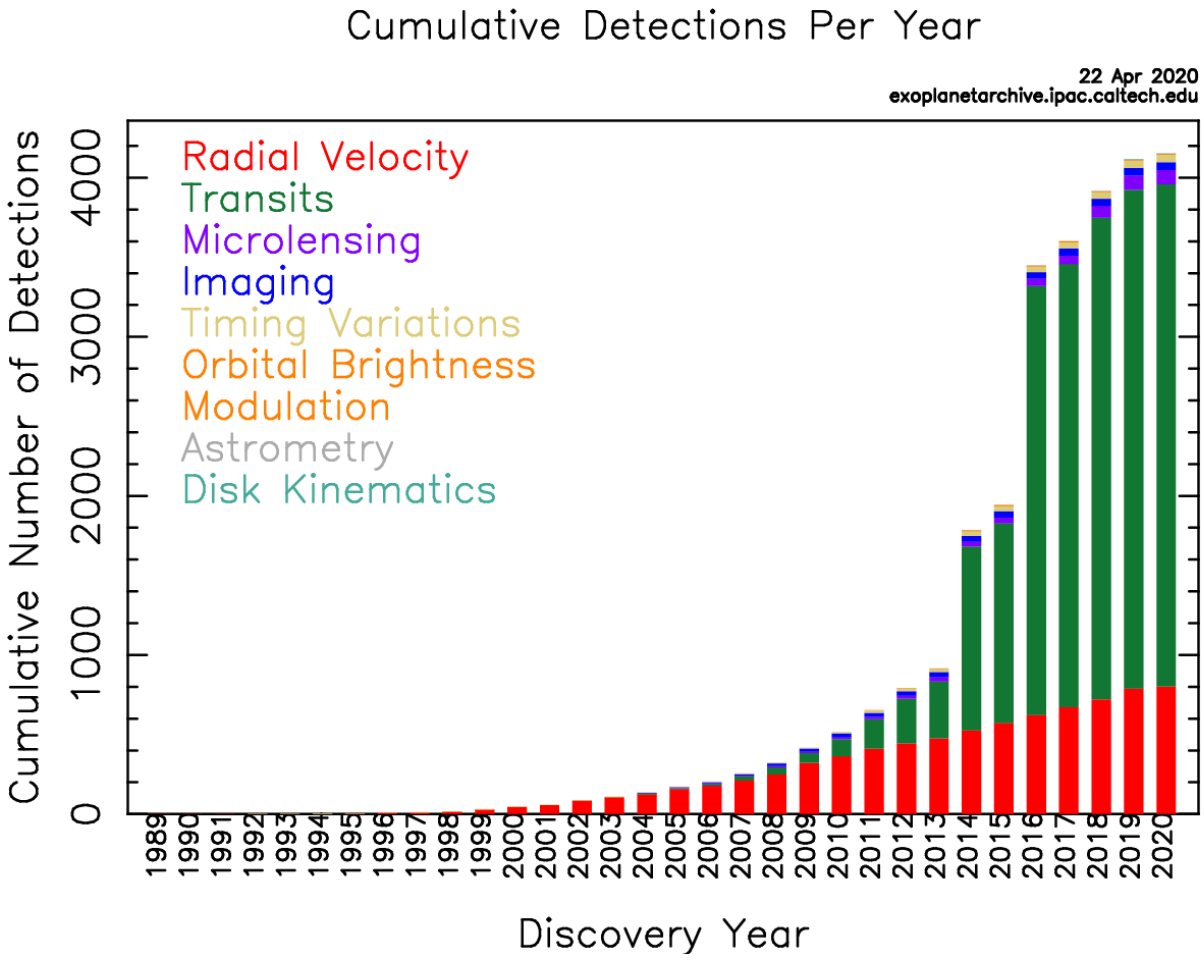

Figure 1.1: A chart showing the number of exoplanets detected per year. Each color represents a different detection method: blue is direct imaging, orange is gravitational microlensing, green is transit, red is radial velocity, and purple is timing variations. Credit: NASA

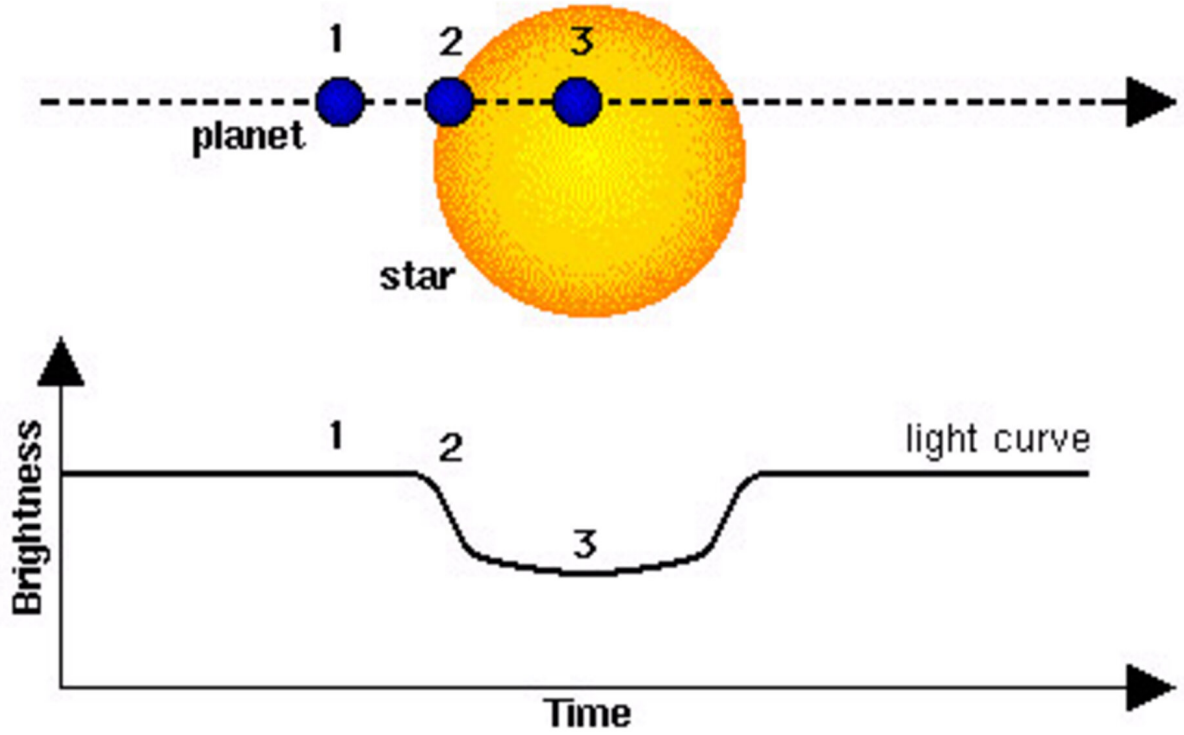

Figure 1.2: A theoretical example illustrating photometric transit detection of an exoplanet. Credit: ESA

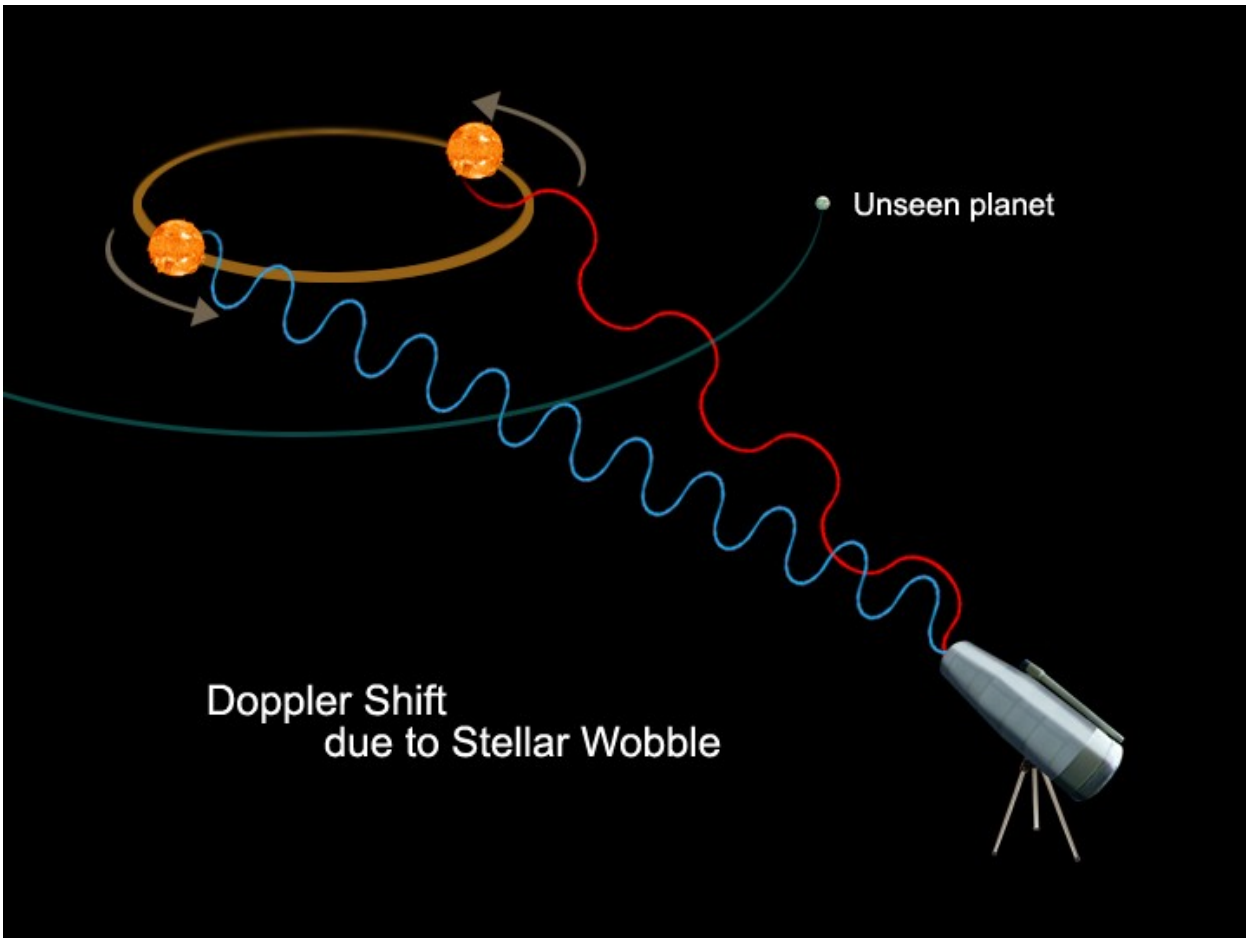

Figure 1.3: A cartoon showing the radial velocity method. Credit: NASA

1.2 Exoplanet Habitability

Life in general is complicated to define and detect. Thus, most studies of exoplanet habitability begin from common ground, the requirement of water for life as we know it. Proceeding directly from this adoption, the habitable zone (Figure 1.4) of a star is defined as the region in which a terrestrial planet *could* support liquid water at its surface (Kopparapu et al., 2014). The limits of this zone depend on the star, orbital (e.g. period, eccentricity) and physical (e.g. radius, mass) parameters of a planet, and the assumed atmospheric constituents of the planet. Because of this, habitable zone limits have been generated for a number of atmospheres to create the optimistic limits generally accepted today (e.g. Kopparapu et al. (2014), Leconte et al. (2013), Ramirez & Kaltenegger (2018))

For transiting exoplanets, one potential method of determining the presence of liquid water is transit spectroscopy. This method utilizes the same principles as transit photometry, except a spectrum of the light passing through the planet's atmosphere is observed. This captures two important pieces of data: atomic and molecular constituents within the observable (i.e. optically thin) outer atmosphere and the depth of those features within the atmosphere. The first is observed through the absorption features of the atmospheric constituents. The second is observed through the wavelength dependent apparent radius of the planet which corresponds to the size of the optically thick portion of the atmosphere; absorption features seen at that wavelength must therefore be above the corresponding atmospheric scale height.

As the atmosphere of most terrestrial exoplanets is difficult to detect, they remain the largest unconstrained source of error in estimating the habitability of a planet. In the

absence of atmospheric measurements, models estimate exoplanet habitability in a variety of ways from the deceptively simple Earth Similarity Index (ESI; Schulze-Makuch et al. (2011)) to one-dimensional photochemical models aiming to predict the molecular and atomic abundances in the atmosphere, to complicated three-dimensional General Circulation Models (GCMs) for analyzing dynamical changes in surface conditions given an atmospheric configuration.

1.3 Dissertation Overview

In this dissertation, I will present my work aiming to probabilistically characterize exoplanet habitability using a suite of models, both one- and three-dimensional. In Chapter 2, I will lay the foundations for this work by prioritizing several TESS planets using a version of the ESI. The most highly prioritized targets from this work then become the targets of the novel statistical methods to estimate primordial water loss laid out in Chapter 3. Finally, in Chapter 4, I apply this same method with a 3D GCM, ROCKE-3D and discuss the habitability of the most Earth-like TESS planet, TOI 700 d. Afterwards I summarize the findings of this work in a brief conclusion.

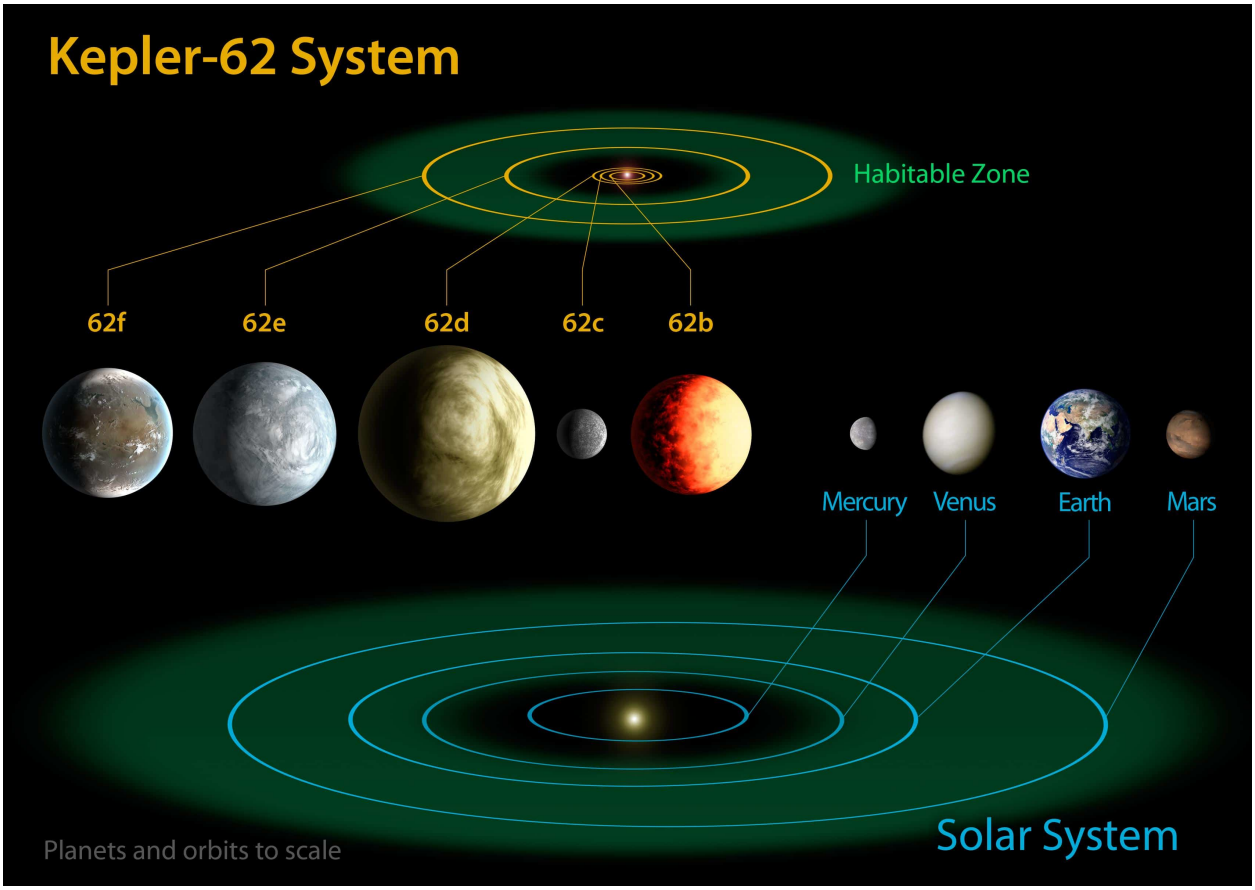

Figure 1.4: An example of the habitable zone for the solar system (bottom) and Kepler-62 (top). Credit: NASA/Ames/JPL-Caltech

2 A General Similarity Index for Prioritizing Follow-Up Observations: Application to TESS Planet Candidates

2.1 Introduction

Nearly 5,200 exoplanets have been confirmed to date. As more targets are detected and confirmed with the Transiting Exoplanet Survey Satellite (TESS) and other telescopes, we will soon have many more interesting targets than the time or resources to observe them. Thus, classification schema are utilized to prioritize targets in order to efficiently further science goals.

Current goals for exoplanets include understanding and characterizing planetary systems, compositions, and environments as well as planetary atmospheres. To this end, new observatories are being created and launched such as JWST and ARIEL for space-based observation alongside a host of ground-based telescopes. Though these observatories will have far surpassed their predecessors in capability and efficiency, observing time is still limited by instrumental constraints, and, especially for transiting exoplanets, the timing of the desirable occurrence to be observed. To aid in prioritizing observational candidates, I have designed a prioritization method that ranks targets according to their similarity to prescribed classifications in any desirable category, the Weighted Generalized Similarity Confidence Method (WGSCM). This method has shown itself to be a fast and accurate way to classify and prioritize thousands of targets based on observational data in terms of science goals.

In section 2 of this chapter, I present the WGSCM, its calculation, and usage as

well as comparisons to other methods. In section 3, I detail the methods used to apply the WGSCM to the TESS Candidate Target List (CTL) to prioritize planet candidates by their likeness to Earth as well as a hypothetical Super-Earth or Mini-Neptune exoplanet in the Habitable Zone. Finally, I discuss the issues with the ESI and WGSCM as well as highlight the strengths of this method over others.

2.2 The Weighted Generalized Similarity Confidence Method

The WGSCM is functionally based on the Earth Similarity Index (ESI; Schulze-Makuch et al. (2011)). Our method involves using this functional form as well as a Markov Chain Monte Carlo (MCMC) sampler to create a pseudo-probability distribution of similarity. This has several distinct advantages over single-input methods such as the ESI and similar indices. Most advantageous is the explicit focus on using experimental and observational data in calculation of the WGSCM which allows for meaningful, robust, and confident prioritizations. This data-based approach is important for efficient and accurate observational follow-up.

In addition, the WGSCM robustly allows and accounts for any distribution type because of its generalized, observation-based input, including very non-Gaussian and heavily uncertain inputs. In contrast, the ESI and similar indices rely on a single parameter for each input category, ignoring the uncertainty and shape of parameter distributions, which is acceptable in cases where the uncertainties are small and well-understood. Transiting exoplanet photometry can exhibit high amounts of uncertainty, especially as planet size decreases, requiring a more robust treatment.

This method is presented first in a general manner, to emphasize its adaptability to

any appropriate situation. The WGSCM is based on the Generalized Similarity Index (GSI), which is a measurement of similarity between two values. The GSI requires a reference range of desired values as well as a reference value with which to compare the similarity of the input parameter. However, if these references can be supplied, the GSI, and thus the WGSCM, can be applied.

2.2.1 The Generalized Similarity Index

The GSI's functional form is based on the ESI:

$$ESI = \prod_{i=1}^{n} \left(1 - \left|\frac{x_i - x_{io}}{x_1 + x_{io}}\right|\right)^{\frac{w_i}{n}} \tag{2.1}$$

where, for a particular planetary property, i, x_i is the input value, x_{i0} is a reference value, and w_i is a weight. The final value for the index is calculated through the weighted geometric mean of the separate indices of the properties of interest. The index has its origin in the Bray-Curtis Similarity Index, most commonly used in ecology to compare species at different sites (Bray & Curtis (1957); Bloom (1981)). In general, this index can be used to determine how similar two datasets are to each other, or in the case of the reformulation used in the GSI or ESI, how close data is to a reference value. In order to utilize the GSI, a range of 'good' values, along with a reference value, must be defined for each parameter. From this reference definition, the weight for each parameter can be calculated by setting the similarity of both limits of the range to 0.8 and solving for the appropriate weight. Since this often yields a different weight for each limit, the final weight is the geometric average of the two

weights. This can be done for each property as follows:

$$w_i = \frac{ln(0.8)}{ln(1 - \left|\frac{x_i - x_{io}}{x_1 + x_{io}}\right|)} \tag{2.2}$$

where x_i is substituted for the lower and upper limits to generate a weight for each limit. The final weight for the parameter is then defined as:

$$w_{final} = \sqrt{w_{lower} * w_{upper}} \tag{2.3}$$

or the geometric average of the two weights.

The use of 0.8 as the limit of similarity is the result of a traditional grouping of similarity ranges where the total defined range of the function is split into 5 groups of similarity (Bloom, 1981) to denote the level of similarity to the reference value. As the GSI's range is 0-1, 0.8-1 represents the highest similarity and thus is why the limits of desired values are defined as having a GSI of 0.8. It is recommended that the parameter limits, not this defined number, be changed if a smaller or larger range of values is desired.

2.2.2 Calculation of the WGSCM

In order to calculate the WGSCM, I utilize the MCMC sampler *emcee* (Foreman-Mackey et al., 2013) to sample a provided parameter distribution 150,000 times. I then use multiproccessing to simultaneously calculate the GSI for each parameter sample as well as the total GSI for the set of samples. If necessary, this process calculates the GSI inputs from the provided datasets, such as calculating density from the provided mass and radius

distributions.

In order to bin these GSI samples, we use the *numpy* histogram function with a total of 100 bins. The density argument is set to True in order to approximate a probability function for the GSI. We interpolate the histogram using the scipy package and finally, integrate by quadrature from 0.8-1. The result of this integration is the Weighted Generalized Similarity Confidence which is a credible interval of the total GSI.

2.3 Applications to the TESS Dataset

TESS was launched in April of 2018 and is currently well into its extended mission. Through its discoveries, TESS is pointing the way for a new generation of telescopes in the process of being readied including the recently launched James Webb Space Telescope as well as a considerable number of ground-based observatories.

The WGSCM method is particularly applicable to this mission as it quickly can prioritize the numerous targets observed by TESS for confirmation and follow-up studies by these new space and ground-based observatories as their observation time will need to be focused. In this section, I will detail applications of the WGSCM to the TESS dataset, focusing on prioritizing the planet candidates (TPCs) identified by the telescope's CTL. I have applied the WGSCM to all TPCs to find their similarity to Earth-sized, super-Earths, and mini-Neptunes in the Habitable Zones of their host stars.

I present first the methods that were used to construct the parameter distributions used in the WGSCM calculations for all candidates as well as which planetary parameters were used in each calculation. Then, for each category of planet candidate, I present the limits and weights used for the GSI calculations of each parameter used. Finally, I present

the top candidates for each category in Table 2 and some example GSI distributions in Figures 1-x. These top candidates will be compared to the scores of solar system objects that relatively fit the categorization.

2.3.1 Parameter Distribution Acquisition

We obtained the input parameter distributions for this survey from the parameter values and uncertainties listed in the TESS CTL produced by the TESS Science Operations Pipeline (TSOC; Stassun et al. (2018)). I assume a Gaussian distribution based on the fitted value and uncertainty. This is not a valid assumption in many cases as non-Gaussian behavior is evident in many fitting procedures (e.g. Kostov et al. (2019)), however, this assumption is made for the purposes of speed as a true treatment of the observations would require a computationally expensive fitting of the data. It is recommended that the planets indicated as priority by our method are fitted in this way, as with the example of TOI 700, in order to more realistically prioritize the candidates.

2.3.2 WGSCM Parameters

For calculating the WGSCM for Earth-likeness, we used the radius, density, surface escape velocity, and insolation. However, for calculating Super-Earth-likeness and Mini-Neptune-likeness, we used the radius, density, and insolation. Surface escape velocity was not used for these WGSCMs as larger planets are likely to retain more primordial atmosphere and thus have significant atmospheres. Determining a 'surface' from a photometric observation of radius would be misleading.

We chose to use insolation, or the power the planets recieve per square meter from

the host star, instead of equilibrium temperature because insolation is calculated based on observable quantities whereas surface temperature is, at best, an educated guess in the absence of atmospheric and surface information. In addition, insolation is frequently used to determine if a planet is in the HZ of its star (e.g. Kopparapu et al. (2014)).

The insolation limits were calculated using the formula:

$$S_{eff} = S_{\odot} + A * T^{*} + B * T^{*2} + C * T^{*3} + D * T^{*4} \tag{2.4}$$

where $T^{*} = T_{eff} - 5780$ is the difference between the host star's effective temperature and the Sun's, $S_{\odot}$ is the S_{eff} value for our own solar system, and the constants a, b, c, and d are the updated coefficients from Ramirez & Kaltenegger (2018). These constants and $S_{\odot}$ change for each limit as shown in Table 1. The inner limit is defined by the increased insolation threshold given by (Leconte et al., 2013) and the outer is the CO2 maximum greenhouse limit from Ramirez & Kaltenegger (2018).

This wide limit ensures fewer assumptions are being made about the potential atmospheres of the TPCs and that all possibilities for the HZ are considered. In order to make the method further sensitive to observational uncertainties, the limits and weight for the insolation are calculated during each sample, drawing values from the fitted stellar temperature distribution. The insolation value for use in the GSI is then calculated by:

$$S = S_{\oplus} \left(\frac{L_{*}}{L_{\odot}} \right) \left(\frac{1AU}{a} \right)^{2} \tag{2.5}$$

where L_{*} is the host star's luminosity, $L_{\oplus}$ is the sun's luminosity, and a is the planet's fitted semi-major axis. Luminosity is calculated from the stellar radius and temperature fits

Constant	Inner Limit	Outer Limit
$S_{\odot}$	1.105	0.3587
A	$1.1921x10^{-4}$	$5.8087x10^{-5}$
B	$9.5932x10^{-9}$	$1.5393x10^{-9}$
C	$-2.6189x10^{-12}$	$-8.3547x10^{-13}$
D	$1.3710x10^{-16}$	$1.0319x10^{-16}$

Table 2.1: Habitable Zone Calculation Coefficients.

for the host star. If data for any of these parameters is notavailable, then this parameter is replaced by the fitted equilibrium temperature with a reference value of 255 K and weight of 5.58 as in the ESI.

The mass of each TPC was estimated using the mass-radius relation by Ning et al. (2018) through the python implementation *mrexo* (Kanodia et al., 2019). This is a non-parametric method that is based on the Kepler dataset. In general, the Kepler dataset has been shown to trend towards rockier and thus denser planets which skews the model, however, new data can easily be added to the model as it becomes available, increasing its predictive confidence. In addition, the wide uncertainties and non-normal distribution of the model make an excellent test of WGSCM robustness.

For the purposes of this survey, the surface escape velocity is determined at the radius of the TPC. This parameter could more accurately be calculated by estimating the actual surface radius or utilizing a GCM to determine the observable radius vs actual surface radius. Unfortunately, using a GCM would take too long, defeating the purpose of this quick prioritization scheme and a surface radius estimate would be quite uncertain.

Finally, for TPCs that have been observed in multiple sectors, we calculate a WGSCM for each sector and then take the geometric average.

2.3.3 Earth-like planets

The specific definitions of what constitutes a generally habitable planet as we know it are inextricably linked to life as we know it, i.e. life on Earth. Thus, the search for habitable exoplanets is a search for relatively Earth-like worlds. Furthermore, detecting an Earth twin has long been the goal of many scientific institutions. Now, with the advent of the next

generation of ground and space observatories, this goal is ever closer to reality. However, TESS is expected to discover a number terrestrial planets and simulation or observation of each would require a great deal of time. Therefore, we have prioritized planet candidates using the GSI according to how near their characteristics are to the Earth's.

2.3.3.1 Parameter Space: Limits and Weights

Limits for the radius were set at 0.8 and 1.25 ($R_{\oplus}$). This yields a weight of 1.89 for the E-GSI. We chose the limits of density and surface escape velocity to agree with the ESI, giving the same weights: 1.07 and 0.7 respectively. The insolation or temperature GSI weights were set as described above.

2.3.4 Super-Earths

Super-Earths are interesting targets for observation for several reasons. As these rocky planets larger than Earth are not found in our solar system, we have no direct observations to rely on for modeling and theory. Therefore, we must draw conclusions about their properties from indirect radial velocity measurements and, hopefully in the future, direct observations of their atmospheres. From an observational standpoint, these planets are better targets than potential Earth twins as their larger size and potentially larger atmospheres are easier to observe, especially around Sun-like stars.

The potential habitability of super-Earths is a tantalizing, even if the question remains distinctly open. A planet only slightly larger than the Earth is expected to retain a significant portion of its primordial volatiles, creating a high-pressure surface inhospitable to more complex life as we know it. However, those super-Earths that spend a significant portion

of their formation time near their host star can lose a significant amount of their extended atmosphere, mainly comprised of these lighter elements (e.g. Luger et al. (2015)). This, coupled with less stellar activity as the star ages, could lead to favorable conditions for life on the surface of one of these planets.

2.3.4.1 Parameter Space: Limits and Weights

The lower limit for the Super-Earth radius was set at 1.25 ($R_\oplus$) for continuity with the upper limit of the E-GSI and the upper limit was set at 1.75 ($R_\oplus$). This upper limit is not quite the limit shown for the existence of rocky bodies of around 2.0 ($R_\oplus$) (Alibert, 2014), but was chosen instead to reflect the observed break between lower and higher radius objects in the Kepler dataset (Fulton et al., 2017). These limits, along with a reference value at the midpoint, 1.5 ($R_\oplus$), result in a weight of 2.54.

Density limits were set to the bulk density of Mars, around 0.791 ($\rho_\oplus$), for the lower limit and the density of pure iron, at around 1.431 ($\rho_\oplus$), for the upper limit with a reference value of the Earth's bulk density. These limits yielded a weight of 1.17. The density limits were chosen to encapsulate the densities of the terrestrial planets of the solar system, however, since the Earth is the densest of these objects, the upper limit was extended to the density of iron to not exclude the possibility of higher density super-earths with small atmospheres.

Finally, the insolation or equilibrium temperature limits and reference values are the same as described above as we still hope to observe habitable conditions on these planets.

2.3.5 Mini-Neptunes

Mini-Neptunes form another interesting classification of exoplanet. Though they have much in common with the gas giants in our solar system, some of these gas dwarfs are expected to have rocky cores (e.g. 2015AsBio..15...57L). In addition, their extended atmospheres are excellent observational targets. Many interesting detections have or are expected to be made, including the relatively recent detections of water in the atmosphere of mini-Neptunes (e.g. Tsiaras et al. (2019)) and the potential for high-atmosphere photochemical hazes (e.g. Crossfield & Kreidberg (2017)).

While we do not expect to find habitable surfaces on these larger, gaseous planets, prioritizing mini-Neptunes in the HZ serves two purposes. Firstly, larger moons, akin to Titan in the solar system, could exist around these gaseous planets with habitable surfaces. In addition, these planets are easier to observe than the super-Earths. Thus, observing these exoplanets allows the community to fine-tune atmospheric detection methods and to make inferences between the planetary composition and other observable parameters of the system.

2.3.5.1 Parameter Space: Limits and Weights

The mini-Neptune lower radius limit was set at 1.75 ($R_{\oplus}$), corresponding again with the observed detection disparity in the Kepler dataset and for continuity with the upper limit of the super-Earth radius range. The upper limit was chosen to be 3.5 ($R_{\oplus}$), well into the gas planet regime and just under the radius of Neptune itself, 3.883 ($R_{\oplus}$). As with the Super-Earth category, the reference value was set to the midpoint of the limits, 2.625. The

weight for the radius, given these values, was 1.20.

Density for this category was chosen to prioritize planets that are mostly gaseous, with limits of 700 kg/m3 and 1700 kg/m3 and a reference value of 1300 kg/m3, corresponding to the densities of Saturn, a bit more than Uranus, and Neptune respectively. Finally, the weight for the density is 1.80. While these densities are low for the smaller planets in this classification, the smallest known exoplanet with a density measurement that might fall into this category, Kepler-138d, would have a GSI of 0.62 for density while mars has a GSI of 0.29. Thus, more terrestrial planets are significantly excluded whereas the denser gas-dominant planets, while not preferred by the index, are not prohibitively excluded.

As with the other categories, the insolation and equilibrium temperature limits and reference values are as described above.

2.4 Discussion and Conclusions

Firstly, as evident from the results in Table Table 2.2, the uncertainty of a system's parameters can affect the WGSCM drastically (e.g. Figures figs. 2.1 to 2.3). Values for Mars and Venus are calculated using single mean values for each parameter, yielding much higher WGSCMs in all categories. Also, for the limits chosen in this work, the WGSCM is weighted more heavily towards lower temperature. Venus has much lower values than Mars because its insolation ($1.9 S_{\oplus}$) is further from Earth's than Mars's ($0.431 S_{\oplus}$) despite Venus having a more similar composition to Earth.

In addition, all individual parameter similarities skew towards the defined reference point, as expected. It can be seen that all candidates have higher super-Earth WGSCMs than Earth WGSCMs as all the candidates are well above Earth in radius.

Target Name	Earth WGSCM	Super-Earth WGSCM	Mini-Neptune WGSCM
TOI 256 b	0.2914	0.5562	0.0921
TOI 203 b	0.1629	0.2412	0.0678
TOI 406 b	0.1137	0.1848	0.0613
Mars	0.6303	0.5398	0.3957
Venus	0.8458	0.7225	0.4356

Table 2.2: The WGSC for each of the most-highly prioritized TOIs is displayed in each of the categories. I have modeled the two best in the Earth-like category (TOIs 256 and 203) along with a temperate terrestrial planet in the TOI 700 system. The WGSC values for Mars and Venus are shown for comparison. Low WGSCs are primarily due to uncertainty in instrumental measurements from TESS.

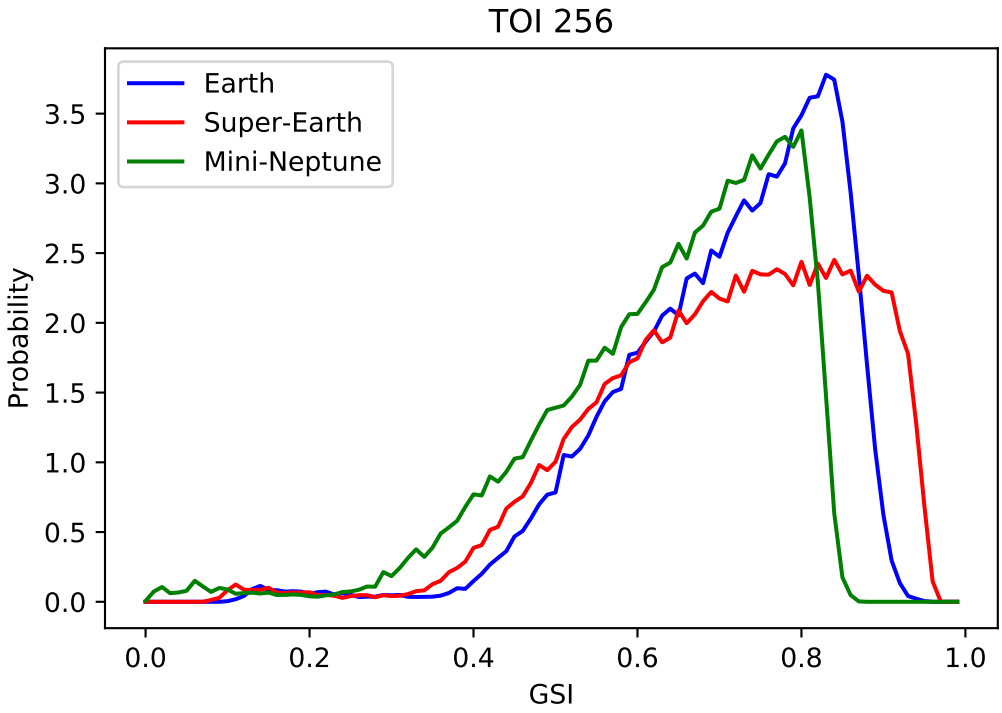

Figure 2.1: The probability of GSI values for the highest priority candidate, TOI 256 b. The similarity to Earth (blue curve) is presented along with the similarity to a super-Earth (red curve) and a mini-Neptune (green curve) with Earth-like insolation

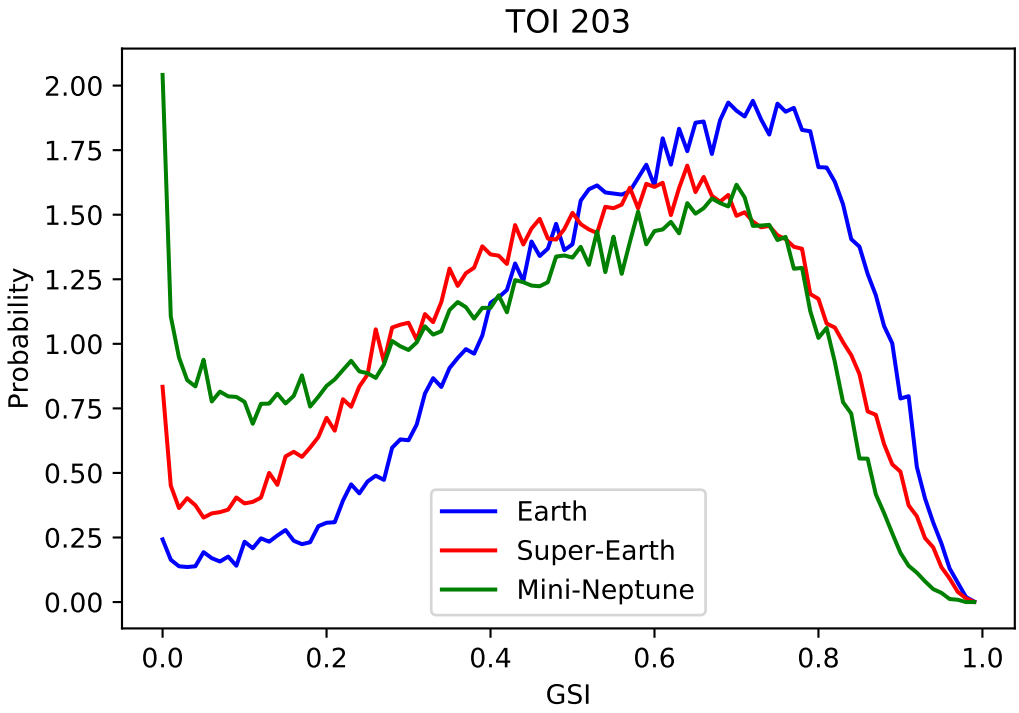

Figure 2.2: The probability of GSI values for the second highest priority candidate, TOI 203 b.

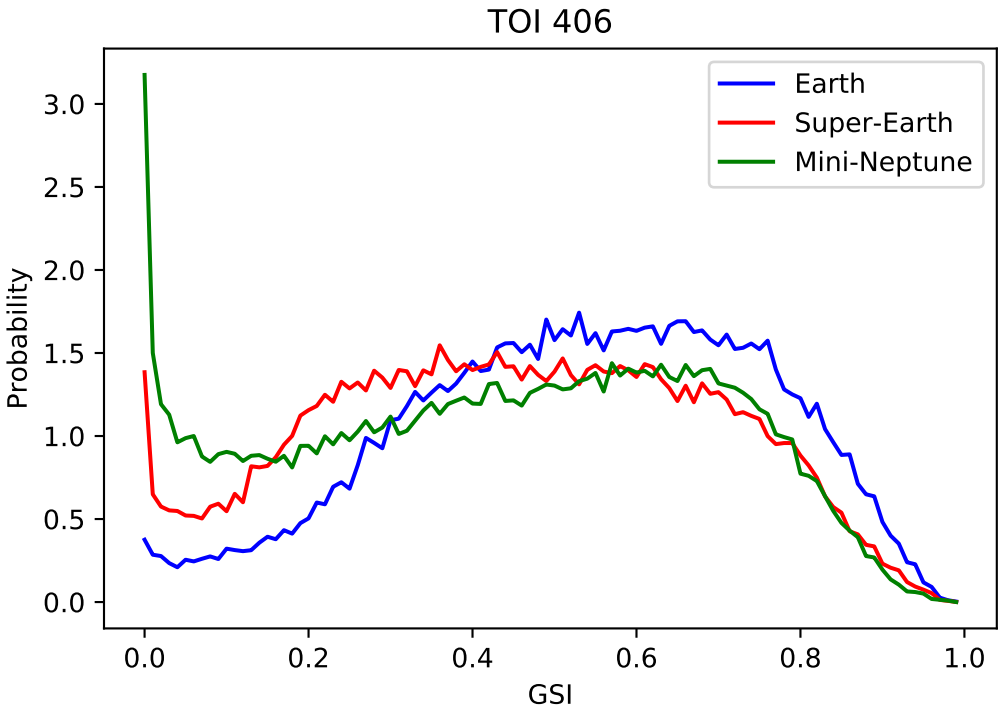

Figure 2.3: The probability of GSI values for the third highest priority candidate, TOI 406 b.

The ESI and WGSCM work more effectively as a first-look prioritization scheme instead of a classification tool. The ESI itself has been shown to not correlate well with planetary habitability, failing to account for, among other things, the activity of the host star, the planet's potential magnetic field (or lack thereof), and tidal locking, any one of which can drastically impact a planet's habitability (e.g. Armstrong et al. (2014), Armstrong et al. (2016)). These parameters could be added into the ESI and WGSCM, however, more complicated caveats (e.g. planetary composition, atmosphere, and magnetic fields) are generally unable to be observed robustly enough on a mass scale. These should be the focus of a followup study using the WGSCM as guidance for target selection as Armstrong et al. (2016) used the ESI to select targets for stellar activity analysis.

In addition, the inherent flexibility of the WGSCM makes it useful for astronomy and science beyond my work. Not only can non-Gaussian distributions be accounted for, new similarities can easily be removed or added to prioritize large data sets to the preferences of the researchers. In fact, two groups may prioritize the same data set with different weights or metrics to identify targets for study that are most interesting to them. The applications to Earth, super-Earth, and mini-Neptunes in this study highlight that flexibility.

I used the WGSCM to order the TESS CTL in the targets' similarity to an Earth, super-Earth, and mini-Neptune in the habitable zone of the targets' host stars. This yielded two interesting Earth-like candidates, TOI 256 b and TOI 203 b, which are the top candidates for Earth-likeness. This first prioritization has led to an orderly examining of the candidates and an initial study of their habitability through primordial water loss along with a candidate fitted improperly for the CTL, TOI 700d.

3 On The Hydrosphere Stability of TESS Targets: Applications to 700 d, 256 b, and 203 b

(The work done in this chapter has been published in the Planetary Science Journal (Bonney & Kennefick, 2022))

Abstract

A main determinant of the habitability of exoplanets is the presence of stable liquid surface water. In an era of abundant possible targets, the potential to find a habitable world remains a driving force in prioritization. We present here a data-forward method to investigate the likelihood of a stable hydrosphere on the timescales of the formation of life, 1 Gyr, and beyond. As our primary application, we use this method to examine the potential hydrospheres of *TESS* Objects of Interest 700 d, 256 b (LHS 1140 b), and 203 b. We first present our selection criteria, which is based on an implementation of the Earth Similarity Index, as well as the results of an initial investigation into the desiccation of the targets, which reveals that TOI 203 b is almost certainly desiccated based on *TESS* observations. We then describe the characterization of the remaining targets and their host stars from *2MASS*, *Gaia*, and *TESS* data and the derivation of sampled probability distributions for their parameters. Following this, we describe our process of simulating the desiccation of the targets' hydrospheres using the *Virtual Planet Simulator*, *VPLanet*, with inputs directly linked to the previously derived probability distributions. We find that 50.86% of the likely cases for TOI 700 d are desiccated and no modeled cases for TOI 256 b are without water.

In addition, we calculate the remaining water inventory for the targets, the percentage of cases that are continuing to lose water, and the rate at which these cases are losing water.

3.1 Introduction

The launch of the *Transiting Exoplanet Survey Satelite* (*TESS*) has built upon the legacy of the Kepler missions, together discovering an astonishing number of exoplanets. This, along with the recently successful launch and commissioning of the *James Webb Space Telescope* (*JWST*), has made the potential discovery of a habitable planet outside of our solar system a more tangible goal.

Unfortunately, the current best chance of robustly assessing the habitability (i.e. stable liquid surface water) of a planet lies with *JWST*, which has significant limitations in both time available as well as resolution of atmospheric spectral signatures for smaller, potentially more Earth-like planets due to their small signal to noise ratio. As such, it is beneficial to prioritize future observations to those which are most likely to produce the most results using as few resources as possible.

Most current methods of prioritization lack proper treatment of the different potential states of the planetary systems they examine (i.e. orbital configuration and planetary composition). Instead, many study only one state or a few (e.g. Barnes et al. (2016); O'Malley-James & Kaltenegger (2017); Becker et al. (2020)) often ignoring the effects of many potentially important parameters, especially mass, which is often poorly constrained in the absence of radial-velocity measurements. A tantalizing option is a grid-based approach to fully capture the intricacies of the parameter space. However, this approach is slow and unwieldy, can easily ignore a number of likely states for the sake of speed, and moreover

is devoid of likelihood information. Indeed, even the study by Fleming et al. (2020) uses pre-prescribed prior distributions instead of observational data. Estimating these parameter distributions severs the link between observations and simulations and requires careful consideration of covariances which are intrinsically captured and propagated in our method.

To this end, we have created a new end-to-end data-forward method of prioritization that is fast and flexible. We utilize Monte Carlo fitting of *TESS* lightcurves to fully analyze the effect of the potential distributions of parameters such as density and insolation on modeling the planets' orbital and atmospheric evolution. This allows us to robustly and thoroughly determine which have the highest chance of being habitable at the present day.

The method leaves room for additional constraints both theoretical and observational. However we present a basic application using only *TESS* data and previously observed stellar parameters.

In this chapter, we describe the selection process of our two targets, *TESS* Objects of Interest (TOIs) 256 b (LHS 1140 b) and 700 d as well as the initial characterization of the targets and their host stars in Section 2. Following this, Section 3 details the specifications for our coupled atmospheric and orbital evolution simulations using the modeling software package *VPlanet* (Barnes et al., 2020) as well as how these simulations are statistically linked to the *TESS* observations. In addition, we present four metrics to assess the degradation of a target planet's hydrosphere within the method. In Section 4, the results of the method are shown for both the initial lightcurve characterization as well as the outcome of the simulations detailed in the previous section. Finally, Section 5 presents our conclusions and recommendations for future observations of both targets.

3.2 Initial Planet Selection & Characterization

Inferring meaningful statistics about the stability of liquid surface water and an Earth-like atmosphere requires accurate and complete parameter distributions for the planets' physical and orbital characteristics. In order to properly simulate these probability distributions, we begin from *TESS*'s 2-minute cadence photometry data on the targets and perform an in-depth data reduction and fit the data using a Monte Carlo method. The resultant traces of each parameter are used in the desiccation simulations. This link between the data and simulations is detailed in Section 3. The reduction of each Target Pixel File (TPF) is handled separately for each sector observation. The resultant lightcurves are then merged and fit following the procedure in section 2.3.

3.2.1 Target Selection

We implemented an adaptation of the Earth Similarity Index (ESI; Schulze-Makuch et al. (2011)) to select targets of interest. The ESI serves as a good basis for our purposes in this study by preferring Earth-like planets in terms of radius and insolation.

Instead of relying on one value for the ESI, however, we used the Markov Chain Monte Carlo (MCMC) sampler *emcee* (Foreman-Mackey et al., 2013) to estimate the likelihood that a target has an ESI of above 0.8. Input parameter distributions were obtained from the Data Validation files produced by the *TESS* Science Operations Pipeline (SPOC; Jenkins et al. (2016)) for all TOIs. The MCMC was sampled using 30 chains of 5000 steps each,resulting in 150,000 samples per parameter (Figure Figure 2.1).

The ESI of each TOI was calculated using the standard formulation except for using

insolation in place of surface temperature. The inner threshold of insolation was set at the values determined by Leconte et al. (2015) to cause a runaway greenhouse effect with the outer threshold being the CO2 maximum greenhouse needed to sustain liquid water (Kopparapu et al., 2014). The three TOIs presented in this study were the top targets for this selection criterion. Additional TOIs have since been discovered, but none have had a higher likelihood of being Earth-like.

Initial *VPlanet* simulations were performed on each planet by sampling the system parameters available from the Exoplanet Follow-up Observing Program (ExoFOP, 2019), assuming a Gaussian distribution, and performing the method described in Section III for the primary atmosphere test. These initial simulations indicated that TOI 203b was almost certainly desiccated: 99.08% of the models that started with 10 Earth Oceans of water ended with no water. The simulations of TOI 700d and 256b, however, only returned 30.35% and 15.18% desiccated models respectively. From these results, we decided to move forward in applying the process detailed herein to TOIs 700d and 256b only.

3.2.2 Host Star Parameterizations

The detection and characterization of transiting exoplanets begins with the host star, and inaccurate measurements of stellar properties have effects at every level of observation and modeling. In order to ensure our targets are accurately modeled, we determine the host stars' radius, mean density, and effective temperature using standard methods in the analysis of M-dwarfs (Berta-Thompson et al. (2015); Dittmann et al. (2017); Ment et al. (2019); Kostov et al. (2019)).

We acquire the measured K-band magnitude and parallax from the *2MASS* (Skrutskie

et al., 2006) and *Gaia* (Gaia Collaboration et al. (2016); Gaia Collaboration et al. (2018); Luri et al. (2018)) surveys, respectively. The input parameters are assumed to be Gaussian, and the uncertainties on output parameters are estimated with a simple Monte Carlo simulation using 200000 samples from the input distributions. The necessary stellar parameters as well as their estimated uncertainties are included in Tables tables 3.1 and 3.2.

The mass of the stellar host is determined using the mass-luminosity relation from Benedict et al. (2016). This mass is then used to estimate the stellar radius using a relationship for single stars (Boyajian et al., 2012) and the mean density is calculated. We estimate the bolometric luminosity as the mean of the corrected K and V magnitudes (Mann et al. (2015), erratum and Pecaut & Mamajek (2013) respectively) and calculate the effective temperature using the Stephan-Boltzmann law. Finally, we confirm these parameters using the (Mann et al., 2019) K-mag-distance-mass relationship.

3.2.3 *TESS* Data Acquisition and Reduction

As with other studies using TESS data (e.g. Gilbert et al. (2020)), we decided to apply a reduction scheme that differs from the standard pipeline. These changes consist of creating a custom photometry aperture for the files, applying reduction and decorrelation techniques while masking transits, and moving the Gaussian process fitting/removal to the data fitting portion. This process necessitates that we begin with the 2-minute cadence TPFs which have undergone an initial cleaning for cosmic rays and flagged observations.

We used the Python program *lightkurve* (Lightkurve Collaboration et al. (2018)) to download the publicly available TPFs and created a custom aperture for each using the threshold method. This method selects pixels that have a flux higher than 3 standard

TOI 256

Parameter	Value	Source
Host Star		
$K_S(mag)$	8.821 ± 0.023	2MASS
$V_J(mag)$	13.10 ± 0.01	Gilbert et al. (2020)
$Parallax(mas)$	66.829 ± 0.048	Gaia DR2
$R_*(R_\odot)$	0.2097 ± 0.00427	This Work
$M_*(M_\odot)$	0.1794 ± 0.00244	This Work
$T_{eff}(K)$	3200 ± 44	This Work
TOI 256 b		
$T_0(BJD - 2457000)$	1399.93 ± 1^a	Exo-FOP
$ln(Period)[days]$	3.208 ± 1^a	Exo-Fop
$ln(TransitDepth)[ppm]$	8.503 ± 0.055	Exo-Fop
TOI 256 c		
$T_0(BJD - 2457000)$	1389.29 ± 1^a	Exo-FOP
$ln(Period)[days]$	1.329 ± 1^a	Exo-Fop
$ln(TransitDepth)[ppm]$	7.832 ± 0.063	Exo-Fop

[a] Variance left at 1 to not over-fit the data

Table 3.1: Model Inputs for TOI 256.

TOI 700

Parameter	Value	Source
Host Star		
$K_S(mag)$	8.634 ± 0.022	2MASS
$V_J(mag)$	14.18 ± 0.03	Dittmann et al. (2017)
$Parallax(mas)$	32.133 ± 0.027	Gaia DR2
$R_*(R_\odot)$	0.4403 ± 0.00937	This Work
$M_*(M_\odot)$	0.4634 ± 0.00464	This Work
$T_{eff}(K)$	3390 ± 44	This Work
TOI 700 b		
$T_0(BJD - 2457000)$	1490.98 ± 1^a	Exo-FOP
$ln(Period)[days]$	2.300 ± 1^a	Exo-Fop
$ln(TransitDepth)[ppm]$	6.221 ± 0.095	Exo-Fop
TOI 700 c		
$T_0(BJD - 2457000)$	1548.75 ± 1^a	Exo-FOP
$ln(Period)[days]$	2.776 ± 1^a	Exo-Fop
$ln(TransitDepth)[ppm]$	8.099 ± 0.073	Exo-Fop
TOI 700 d		
$T_0(BJD - 2457000)$	1742.15 ± 1^a	Exo-FOP
$ln(Period)[days]$	3.622 ± 1^a	Exo-Fop
$ln(TransitDepth)[ppm]$	6.418 ± 0.073	Exo-Fop

[a] Variance left at 1 to not over-fit the data

Table 3.2: Model Inputs for TOI 700.

deviations above the median brightness and are contiguous with the center pixel. Each aperture is visually inspected to ensure that it includes only the target star and is devoid of other contamination.

To avoid overcorrecting the data during transit, each TPF is then masked for the duration of each planet's transit(s) with room for error. Expected transit times and lengths as well as the variance for each are taken from Exo-FOP and are included in Tables tables 3.1 and 3.2.

Using the pixel and time series masks, we perform a pixel-level decorrelation on each TPF using the built-in method in *lightkurve*. Finally, we extract each lightcurve from the TPFs, remove NaNs and outliers $> 7\sigma$ outside of expected transits, and normalize the lightcurves. An example of the final, cleaned lightcurve is given in Figure Figure 3.1.

Lightcurves for each sector's observation are cleaned separately. The entire catalogue of observations of TOI 256 were used, but only the first 11 sectors' observations were used for TOI 700 to be consistent with the data used in Gilbert et al. (2020) and Suissa et al. (2020).

Finally, the lightcurves for each sectors' observation are stitched together based on the average of the error in the lightcurve. The lightcurves for TOI 256 had similar error and are stitched together before fitting. As TOI 700 has some differences in error between sectors, the sectors were grouped together into 4 groups: sectors 1, 3, 4, and 5 form group 1, sectors 6 and 7 form group 2, sectors 8 and 9 form group 3, and sectors 10, 11, and 13 form group 4.

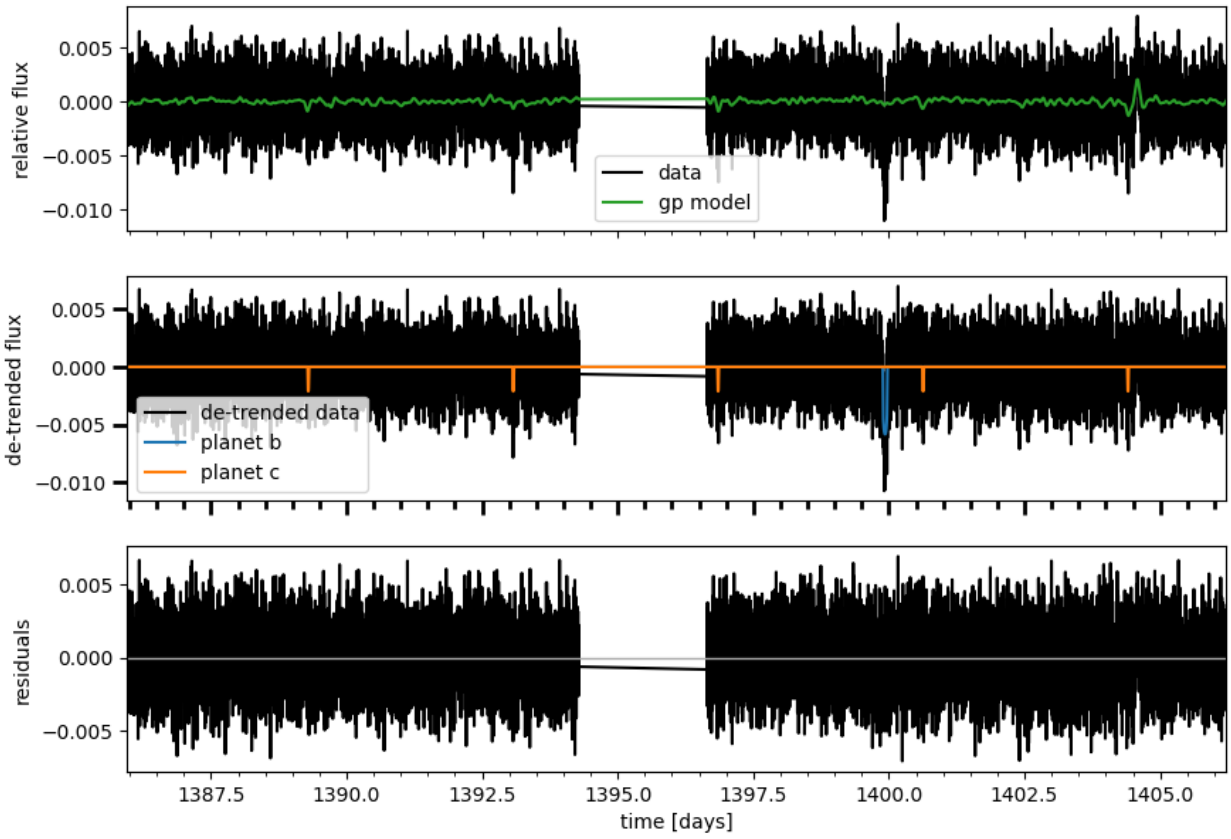

Figure 3.1: TESS lightcurve for TOI 256 cleaned for instrument systematics and normalized (upper panel) showing the Gaussian Process (GP) model (green curve), lightcurve minus the GP model (middle panel) showing the exoplanet transit model for planets b (blue curve) and c (orange curve), and the residual data with the GP and transit models subtracted (bottom panel).

3.2.4 Lightcurve Fitting and Analysis

The reduced and extracted lightcurves are fit for transits using exoplanet and its dependencies (Foreman-Mackey et al. (2021); Salvatier et al. (2016); The Theano Development Team et al. (2016); Kumar et al. (2019); Astropy Collaboration et al. (2018); Luger et al. (2019); Foreman-Mackey et al. (2017)). The stellar mass and radius are parameterized via a normal distribution bounded above 0. Limb-darkening parameters are estimated in-model following (Kipping, 2013a) and were sampled uniformly. The impact parameters were sampled uniformly between zero (the center of the star) and one plus the planet-to-star radius ratio for each planet (the edge of transit overlap). We used a beta distribution as a prior on the eccentricities as suggested by Kipping (2013b), bounded between zero and one. The periastron angle was sampled randomly. Transit depths and periods were parameterized using their natural logs. All other system parameters are modeled using a Gaussian distribution.

The list of parameters included in the fit as well as the values is available in Tables tables 3.1 and 3.2. Parameters described above that are not included in the table had random initial values. Variance for some parameters in the prior distributions is intentionally left high so as to not unduly influence the fitting procedure.

To model noise, we fit a Gaussian process (GP) that is a mixture of two simple harmonic oscillators comprised of two hyperparameters, $ln(\rho_{GP})$ and $ln(\sigma_{GP})$ as well as a mean flux offset, μ_F, and the natural log of the variance, $ln(\sigma_F)$. The initial value for μ_F is 0 and $ln(\sigma_F)$ is calculated from the variance of the flux with transits masked. The initial value for $ln(\sigma_{GP})$ is set to be $ln(\sigma_F)$, and $ln(\rho_{GP})$ is initially 0. Variance for the noise parameters is set at 10 for each value to allow adequate flexibility in the modeling process.

We first run the parameters through the version of the *PyMC3* (Salvatier et al. (2016)) optimization routine which was made for use with *exoplanet*. The initial transit lightcurves for each planet are plotted along with the Gaussian process model and residual (Figure Figure 3.1) and are visually inspected to confirm the model transits line up with the observed lightcurve. In addition, the optimization solution is inspected for significant deviations from the expected parameters as this can indicate that the model is incorrect and must be changed. In practice, changes are made if the median values differ from expected by more than a standard deviation, the errors are abnormally large, or the model chains do not converge.

After the initial model is inspected, a mask is created for data outside 5σ of the residual mean. This secondary data clipping enables more accuracy in the Gaussian process modeling, resulting in a more accurate lightcurve fit.

The resulting lightcurve is used in a second optimization of the parameters which yields a final model to be sampled using the No U-turn Sampler (Hoffman & Gelman (2011)). We use 4 chains with 6000 tuning steps and 5000 draw steps each, yielding a trace of 20000 steps total. For all traces, the Gelman-Rubin diagnostic (Gelman & Rubin (1992)) was near 1.0 and the number of effective samples was over 1000 for all parameters. The sampled traces are saved as fits files and are available upon request. Section 4 shows the deterministic parameters computed as part of this sampling as well as their median and variance.

3.3 Desiccation Simulations

A major concern of exoplanet habitability is the ability to sustain liquid water at the surface long enough for life to have the chance to form, especially around smaller (i.e.

M-dwarf) stars (Luger & Barnes (2014)). These smaller stars tend to actively flare well into their lives, spewing dangerous amounts of XUV radiation that can destroy water and lead to the total desiccation of their satellites (Reid (2005); Scalo et al. (2007)).

On Earth, our one data point for life, the period between the formation of the oceans and the initial stage of life is estimated to be at most 770 Myr and as little as 260 Myr (Dodd et al. (2017)). Because of the activity level of M-dwarf stars, however, we will investigate whether or not the hydrosphere is stable up to 1 Gyr after the system forms. Though we cannot say for certain if life has or will evolve on the targets, this time period samples Earth-like timescales for life evolution while allowing for the greater activity likely around M-dwarfs.

For each parameter set in the trace obtained by the methods in Section 2, we instantiate and execute two *VPlanet* simulations of orbital, rotational, and atmospheric evolution using the *stellar*, *atmesc*, and *eqtide* modules. The first of the two simulations assumes the planet formed roughly 1 Myr after the star and integrates until 1 Gyr. This choice is made to line up with the lower limit of predicted proto-planetary disk lifetimes of 1Myr to 10 Myr (Walter et al. (1988); Strom et al. (1989)). This is intentionally before the lower limits on theoretical predictions of the *in situ* formation of our solar system's terrestrial planets (Chambers (2004), Kleine et al. (2009), Raymond et al. (2014)) to allow for more erosion of the hydrosphere over the course of the simulations, producing a more conservative result. The second simulation takes the system environment as it has been recently observed and models the next Gyr. Both simulations address the issue of hydrosphere stability, focusing on primary and secondary atmospheres, respectively.

3.3.1 VPlanet Setup and Assumptions

Before setting up the input files, we estimate the planet mass using the non-parametric method from Ning et al. (2018). We use the *mrexo* package for python (Kanodia et al. (2019)) with the option to generate a complimentary MCMC trace for a posterior sample of the target planets' radii (Figure Figure 3.2). A practical example can be seen in (Figure Figure 3.3) for TOI 256 b. This naive approximation can be replaced with the resultant probability distribution from simultaneously fitting transit and radial-velocity measurements for more accurate simulations. We instead utilize this naive approach to highlight the potential insights gained from photometric transit data alone.

The *atmesc* model uses a simple, energy-limited atmospheric escape model (Watson et al. (1981)) based on investigations of the solar wind by Parker (1964):

$$F_{EL} = \frac{\epsilon_{XUV} \mathcal{F}_{XUV} R_p}{4 G M_p K_{tide} m_H} \tag{3.1}$$

where $\mathcal{F}_{XUV}$ is the XUV energy flux, M_p is the mass of the planet, R_p is the planet radius, $\epsilon_{XUV} \approx 0.1$ is the initial XUV absorption efficiency, and K_{tide} is a tidal correction term of order unity (Erkaev et al. (2007)). This model is an inferred trend in atmospheric escape as a function of planet size and irradiation based on statistical studies of all known exoplanets (Owen & Wu (2013); Lopez & Rice (2018)). It is applied to these targets as an estimate in absence of specific knowledge of their individual atmospheric escape processes, especially over such a large mass range. We allow ϵ_{XUV} to vary over the lifetime of the star as in Bolmont et al. (2016). This quantity is integrated over the planet's effective radius to incoming XUV

energy:

$$R_{XUV} = \frac{R_p^2}{H \log(p_{XUV}/p_s) + R_p} \tag{3.2}$$

(Lehmer & Catling (2017)), where H is the atmospheric scale height, p_{XUV} is the pressure at the effective XUV absorption level, and p_s is the pressure at the surface.

As fluctuation in the stellar luminosity can greatly affect the model output, we chose to use the accepted values of $0.0233 L_\odot$ for TOI 700 and $0.00441 L_\odot$ for TOI 256 instead of the trace values. Current stellar age is also taken to be the accepted values of 1.5 Gyr and 5 Gyr respectively. The radius and mass (and thus the density) are fixed to the average values of the trace. The *stellar* module interpolates over the mass and time of the Baraffe et al. (2015) evolutionary tracks and the XUV luminosity is tracked using the broken power law model of Ribas et al (2005):

$$\frac{L_{XUV}}{L_{bol}} = \begin{cases} f_{sat} & t \leq \tau \\ f_{sat}\left(\frac{t}{t_{sat}}\right)^{-\beta_{XUV}} & t > \tau \end{cases} \tag{3.3}$$

As is standard in these simulations for M-dwarf type stars, we use $f_{sat} = 1e-3$ for the saturation phase ratio, $\tau = 1Gyr$, and $\beta_{XUV} = -1.23$ for the power law exponent which is in this case set for Sun-like (smaller) stars (Ribas et al. (2005)).

We assume that the planet has no hydrogen/helium envelope as this is eroded in the model before water loss begins. In this case, the model assumes that atmospheric escape only takes place if the planet enters the runaway greenhouse threshold (Kopparapu et al. (2013)). In this case, the surface temperature exceeds $647K$, fully evaporating surface oceans and leading to a water vapor dominated upper atmosphere (e.g., Kasting (1988)).

Efficient oxygen sinks are turned on in the model we use. This instantly removes photolytically produced oxygen from the atmosphere, preventing it from building up. This raises the threshold for the diffusion-limited flux of oxygen atoms through the background atmosphere of hydrogen:

$$F_{diff} = \frac{(m_O - m_H)(1 - X_O) b_{diff} g m_H}{k_{boltz} T_{flow}} \tag{3.4}$$

which is the limit above which the model adjusts the energy-limited flux equation as follows:

$$F_{EL} \left(1 + \frac{X_O}{1 - X_O} \frac{m_O}{m_H} \frac{m_c - m_O}{m_c - m_H} \right)^{-1} \tag{3.5}$$

where m_c is the crossover mass, the largest particle mass that can be dragged through the outflow:

$$m_c = \frac{1 + \frac{m_O^2}{m_H^2} \frac{X_O}{1 - X_O}}{1 + \frac{m_O}{m_H} \frac{X_O}{1 - X_O}} m_H + \frac{k_{boltz} T_{flow} F_H^{ref}}{\left(1 + X_O \left(\frac{m_O}{m_H} - 1 \right) \right) b_{diff} g} \tag{3.6}$$

In the equations above, m_H is the mass of the hydrogen atoms, m_O is the mass of the oxygen atoms, k_{boltz} is the Boltzmann constant, $T_{flow} = 400K$ is the temperature of the hydrodynamic flow (Hunten et al. (1987); Chassefière (1996)), $b_{diff} = 4.8x10^{17} (T_{flow}/K)^{0.75} cm^{-1} s^{-1}$ is the binary diffusion ratio for the two species (Zahnle & Kasting (1986)), g is the planet's acceleration due to gravity, and X_O is the molar mixing ratio of oxygen at the base of the flow.

This model for determining hydrosphere degradation is a very approximate description and neglects to include many key factors in the loss of an atmosphere, such as the

wavelength-dependant nature of heating the upper atmosphere and any non-thermal escape processes (e.g. flares). In addition, other photochemical and 3D hydrodynamic processes within the atmosphere can alter the rate of outflow. However, several statistical studies have shown that the escape rate scales with the stellar XUV flux and inversely with the gravitational potential energy of the gas (e.g. Lopez et al. (2012); Lammer et al. (2013); Lopez & Rice (2018); Owen & Wu (2013); Owen & Wu (2017)). The uncertainties regarding physics and the specifics of each planet are folded into the XUV escape efficiency $\epsilon_{XUV} \approx 0.1$ which has predict the correct escape fluxes within a reasonable margin in these studies. The lack of specific information necessary to accurately model hydrodynamic escape necessitates the use of this kind of model for the purposes of our method which aims to prioritize targets for followup observations to obtain this information.

In order to simulate the hydrosphere degradation during the active phase of the star, we assign the initial water on the simulated planet to be 10 Earth Oceans as in Luger & Barnes (2014) for their most water-rich case. As we lack planetary formation and migration information of the target systems, their initial water inventory is difficult to ascertain. However, Earth is thought to have formed and accreted up to 70 oceans worth of water (Morbidelli et al. (2000); Raymond et al. (2006); Chassefière et al. (2012)), making this a conservative estimate for initial water inventory.

The stability of a secondary hydrosphere is tested by setting the initial water inventory in Earth oceans to be proportional to the planet's mass in Earth masses. This tests the possibility that the planets can currently support a proportional amount of stable water for a long time and thus retain any primary or secondary hydrosphere for long enough that life could develop. Neither method is intended to be a definitive judgement of the planets'

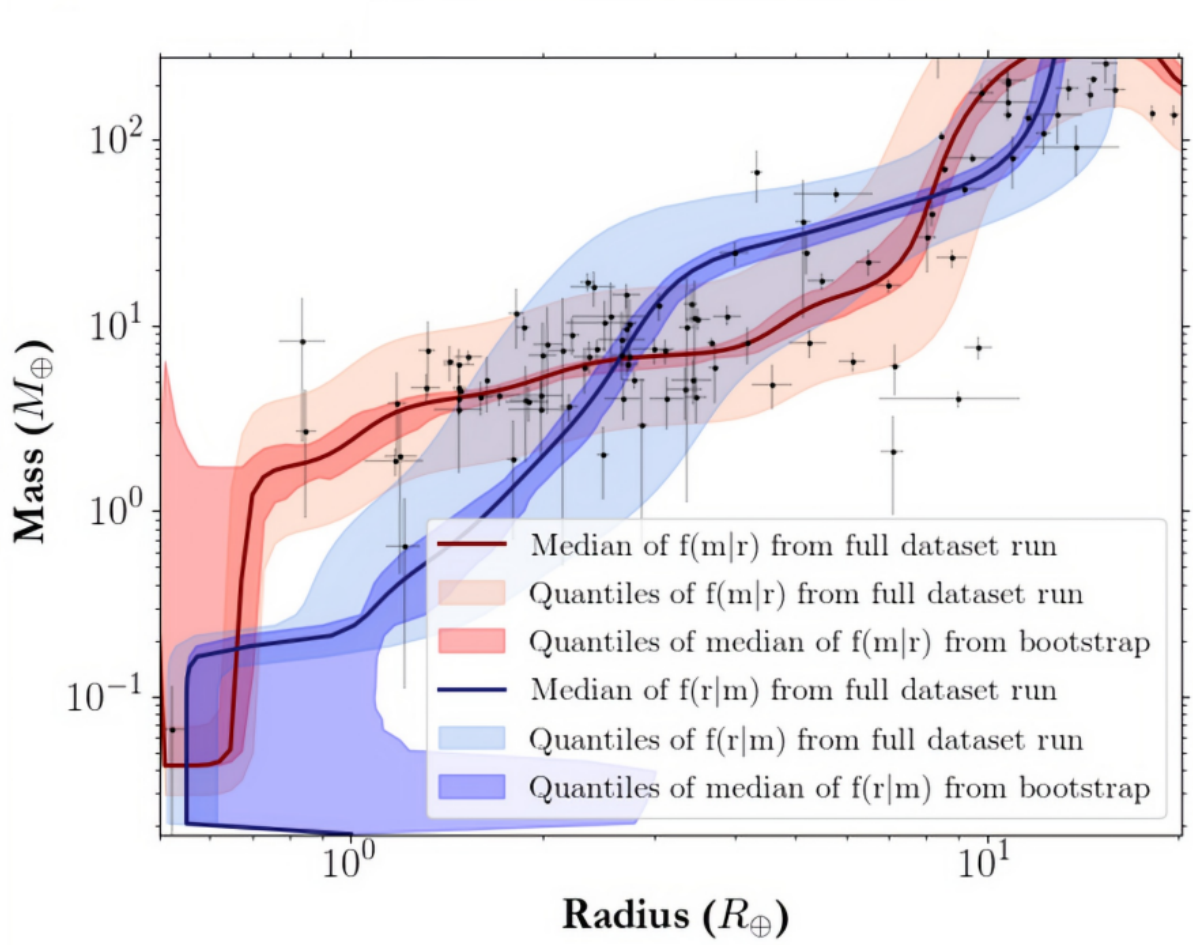

Figure 3.2: Figure adapted from Kanodia et al. (2019) highlighting the nonparametric fit for mass given radius used in this work shown in red. The accompanying fit for radius given mass is also shown in blue. The mean of the fits is shown as a dark line and the shaded regions show the 16% and 84% quantiles for the conditional distributions. Data used in this fitting are from the Kepler dataset.

habitability.

The simulation results are given in Section 4. For statistics relating to TOI 700 d, the parameters are weighted according to the number of data points in their respective lightcurves. The output files and aggregate files of the final parameters are available upon request.

3.3.2 Desiccation Metrics

We use four desiccation metrics to analyze the *VPlanet* outputs: desiccation percentage, remaining water inventory, percent of static models, and non-static desiccation rate. The necessary components of each metric are calculated during the data aggregation phase along with the results presented in Section 4.

3.3.2.1 Desiccation Percentage

This metric is simply calculated by dividing the number of simulations that become completely desiccated by the total number of simulations. As the uncertainty relating to the fitted parameters could be relatively large, this metric gives a simple first glance at the sustainability of the hydrosphere across the parameter space. Desiccation percentage is mostly applicable to primary hydrosphere degradation as this is when the bulk of water is lost in the simulations.

3.3.2.2 Remaining Water Inventory

The remaining water inventory is calculated from the water mass of the final time step in the simulation. For the set of simulations starting with 10 Earth oceans of water,

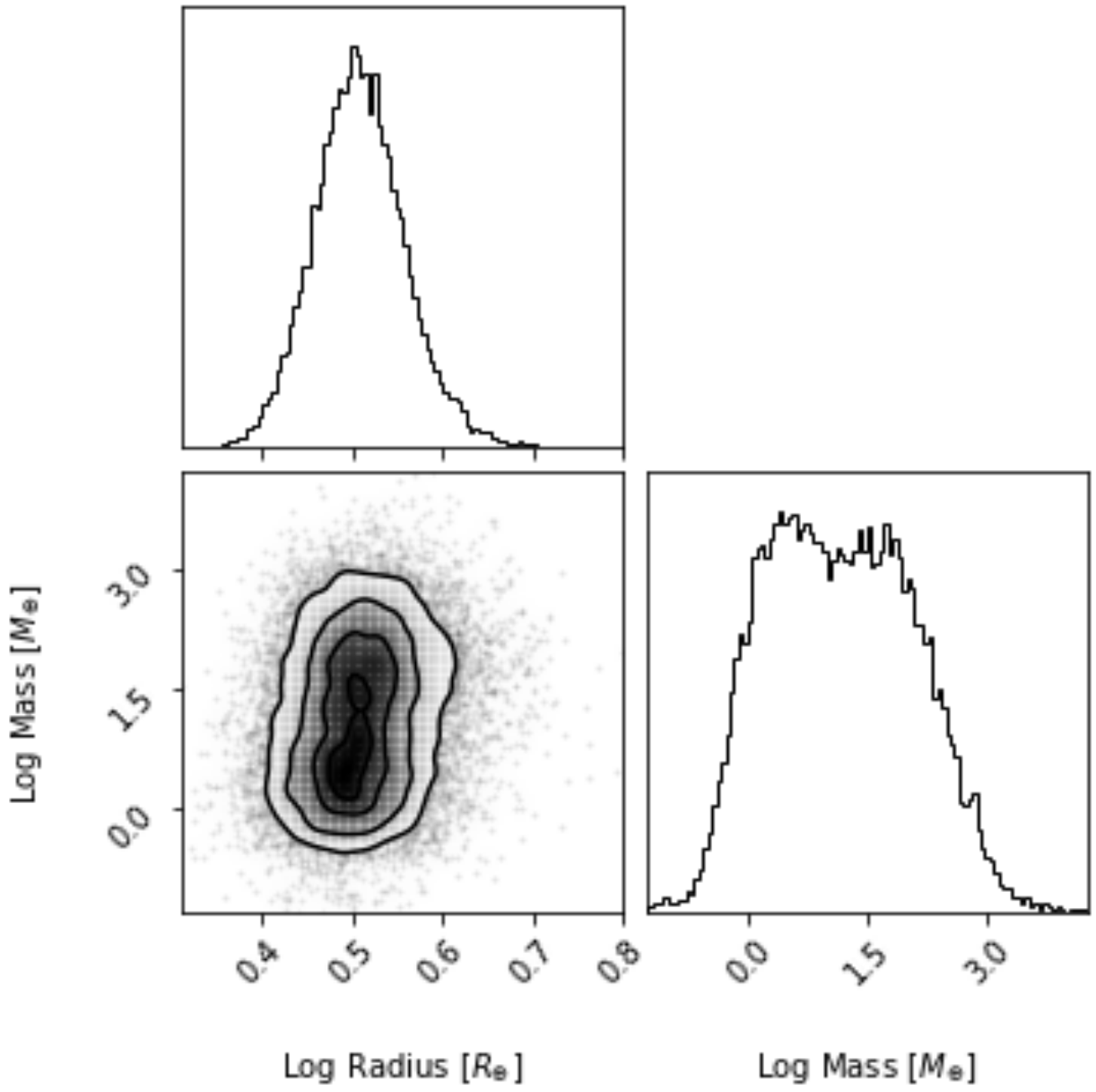

Figure 3.3: Log radius (upper left panel) from the TESS data fitting, log mass given this radius distribution (bottom right panel), and their 2D probability distribution (bottom left panel) showing the bimodality of the mass fitting.

the metric is taken to be this final value. This is instead expressed as a percentage of the original water mass for the secondary simulations with proportional initial water.

Two versions of this metric are presented here: one including desiccated cases and one that does not. Including desiccated cases essentially yields a reflection of the desiccation percentage metric, while rejecting desiccated cases explores not only the final water distribution in hydrated cases, but, more importantly, what the expected amount of water is given water is discovered on the target.

3.3.2.3 Static Cases

The static case percentage tracks how many of the final model states have ceased losing water. As desiccated models would inherently be static, they are excluded. To calculate the metric, the difference of water present in the final two steps of non-desiccated models is taken and counted if it is zero. After the aggregation is finished, the final count of static cases is divided by the number of non-desiccated models to form the metric. This reveals the stability of the planets' overall hydrosphere, should one exist, which is important for determining longer-term sustainability.

3.3.2.4 Non-Static Desiccation Rate

Finally, for those models that are losing water, we take a derivative 1 Myr from the stop time to determine the final desiccation rate. This is a fairly selective metric as in both systems the majority of cases were static, however, in more active systems, this metric is important to determine the likelihood of complete desiccation at the present time.

3.4 Results

3.4.1 System Parameters

In this section, we present the deterministic parameters computed by sampling the resultant trace of fitting *TESS* lightcurves for TOIs 700 and 256 as well as their median and variance. In addition, the naive mass prediction for each planet is given.

TOIs 700d and 256 b have posterior predicted periods of $P_{700d} = 37.406^{+0.067}_{-0.061}$ days and $P_{256b} = 24.737^{+6.33e-5}_{-6.12e-5}$ days and posterior predicted radii of $R_{700d} = 1.123^{+0.131}_{-0.114}$ $R_\oplus$ and $R_{256b} = 1.650^{+0.087}_{-0.078}$ $R_\oplus$ respectively. The results of the fit are well in-line with other studies using *TESS* data (Gilbert et al. (2020); Lillo-Box et al. (2020); ExoFOP (2019)). Gilbert et al. (2020) and Lillo-Box et al. (2020) use other observations to model stellar variability from the All-Sky Automated Survey for Supernovae (ASASSn) and HARPS + ESPRESSO respectively, leading to small discrepancies between their studies and this work.

From radial velocity observations, the mass of TOI 256 b is known to be $M_{256b} = 6.48 \pm 0.46 M_{oplus}$ (Lillo-Box et al. (2020)), well within the standard error on our naive prediction, presented in Table **??** and table 3.4, which also considers the potential for the target to be gaseous. The effect of the bimodal mass predictions is evident in Figures Figure 3.4 and Figure 3.5 where the predicted density has a degeneracy with predicted water loss. The values given here and used in the simulations serve as examples for the use of this method when radial velocity measurements are not available.

Parameter	TOI 256 Median	-1σ	$+1\sigma$
TOI 256 b			
Period (days)	24.737	$6.1e-5$	$6.3e-5$
Radius ($R_\oplus$)	1.650	0.078	0.087
$T_0(BJD-2457000)$	1399.929	0.001	0.001
Impact Parameter	0.269	0.188	0.232
$ln(depth)[ppm]$	8.806	0.053	0.052
Mass ($M_\oplus$)	2.320	1.822	5.221
Mass (from log; $M_\oplus$)	2.847	1.746	4.928
TOI 256 c			
Period (days)	3.778	$6e-6$	$6.1e-6$
Radius ($R_\oplus$)	1.155	0.057	0.063
$T_0(BJD-2457000)$	1389.293	0.001	0.001
Impact Parameter	0.237	0.173	0.267
$ln(depth)[ppm]$	8.103	0.055	0.054
Mass ($M_\oplus$)	1.103	0.700	1.445
Mass (from log; $M_\oplus$)	1.413	0.636	1.371

Table 3.3: Derived planet parameters for the TOI 256 system.

TOI 700			
Parameter	Median	-1σ	$+1\sigma$
TOI 700 b			
Period (days)	9.977	0.003	0.019
Radius ($R_\oplus$)	0.980	0.090	0.091
$T_0(BJD - 2457000)$	1331.263	0.065	0.075
Impact Parameter	0.242	0.176	0.262
$ln(depth)[ppm]$	6.276	0.140	0.136
Mass $M_\oplus$	0.840	0.577	1.257
Mass (from log; $M_\oplus$)	1.206	0.733	1.199
TOI 700 c			
Period (days)	16.045	0.006	0.005
Radius ($R_\oplus$)	2.975	0.185	0.271
$T_0(BJD - 2457000)$	1339.991	0.084	0.072
Impact Parameter	0.908	0.020	0.018
$ln(depth)[ppm]$	8.061	0.047	0.050
Mass $M_\oplus$	5.377	4.392	12.072
Mass (from log; $M_\oplus$)	7.480	4.043	11.273
TOI 700 d			
Period (days)	37.406	0.062	0.068
Radius ($R_\oplus$)	1.123	0.114	0.131
$T_0(BJD - 2457000)$	1330.401	0.560	0.485
Impact Parameter	0.424	0.278	0.233
$ln(depth)[ppm]$	6.501	0.166	0.167
Mass $M_\oplus$	0.922	0.660	1.575
Mass (from log; $M_\oplus$)	1.404	0.681	1.492

Table 3.4: Derived planet parameters for the TOI 700 system.

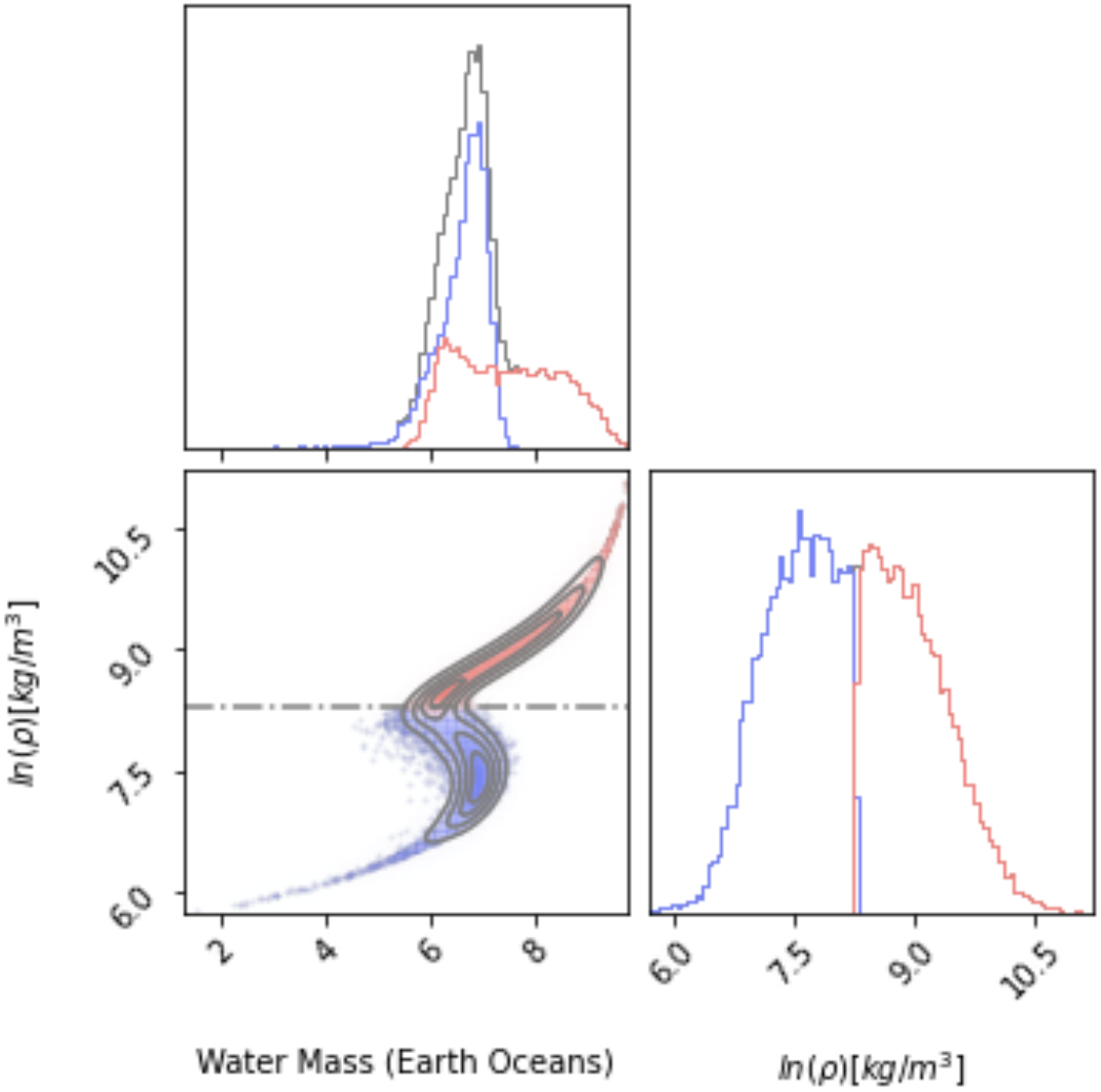

Figure 3.4: Remaining water mass (upper left panel), natural log of the predicted density (bottom right panel), and their 2D probability distribution (bottom left) for TOI 256 b. The data is split into higher density (pink) and lower density (blue) for all panels using the density of Mars (horizontal line in bottom left panel) as the dividing factor. The increase in water retention below the density division is due to the implied presence of an extended gaseous envelope. As the observed natural log density of TOI 256 b is approximately 8.96 (Lillo-Box et al. (2020)), we predict that it will retain most of its initial water inventory.

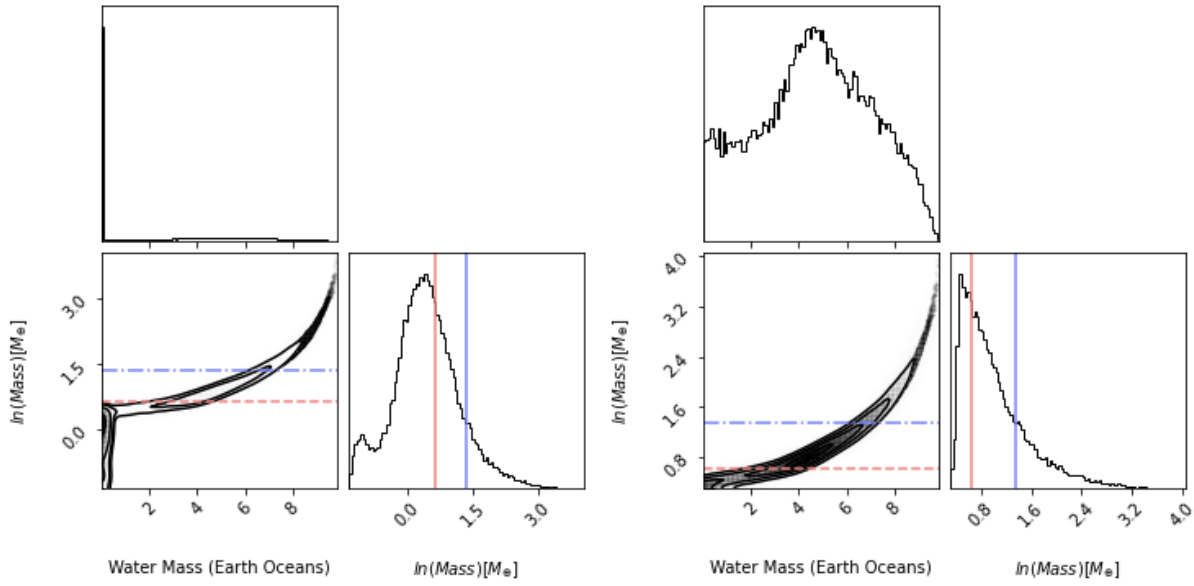

Figure 3.5: Both corner plots highlight remaining water mass (upper left panel), natural log of the predicted mass (bottom right panel), and their 2D probability distribution (bottom left) for TOI 700 d. The predicted mass using the density of mars is shown by the pink line and the predicted mass using the mass-radius relationship of Sotin et al. (2007) is shown by the blue line. The left set of panels includes fully desiccated models whereas the right set is constructed from models that retain some water. If the planet is of a terrestrial density (i.e. as predicted by Sotin et al. (2007)), then we expect that it will lose little of its primordial water while in the runaway greenhouse phase of evolution.

3.4.2 Desiccation Metrics

We present the desiccation metrics for TOIs 700 d and 256 b in Table Table 3.5 as well as the correlation between water loss and density in Figures Figure 3.4 and Figure 3.5. In many cases, both targets appear to be able to maintain a stable hydrosphere which is a strong predictor for their habitability; all cases with terrestrial densities retain some water.

For all planets in the target systems, modern simulations using proportional water inventories resulted in no water loss. This is due in majority to the low activity levels of the host stars, resulting in low XUV flux which did not trigger runaway greenhouse effects and thus water loss in the model. Thus, these results are not presented in Table Table 3.5. Unfortunately, no other planet besides the two targets shown in Table Table 3.5 had more than 1% of their simulations conclude with remaining water. In addition, of those that retained water, none had any static cases, meaning their hydrospheres would be predicted to degrade until fully desiccated. They are excluded from the table for this reason.

Desiccated models are included when calculating remaining water inventory statistics, resulting in a peak in the distribution at zero. Because of this, the desiccation percent is a more useful metric for assessing the stability of a primary/formation hydrosphere. As expected, the planets that are safely in the habitable zone have the fewest desiccated cases and retain the most water.

3.4.2.1 TOI 700 d

As just over 50% of models for TOI 700 d returned a desiccated state, the median value of remaining water mass is 0 Earth oceans. For this reason, we also present this metric

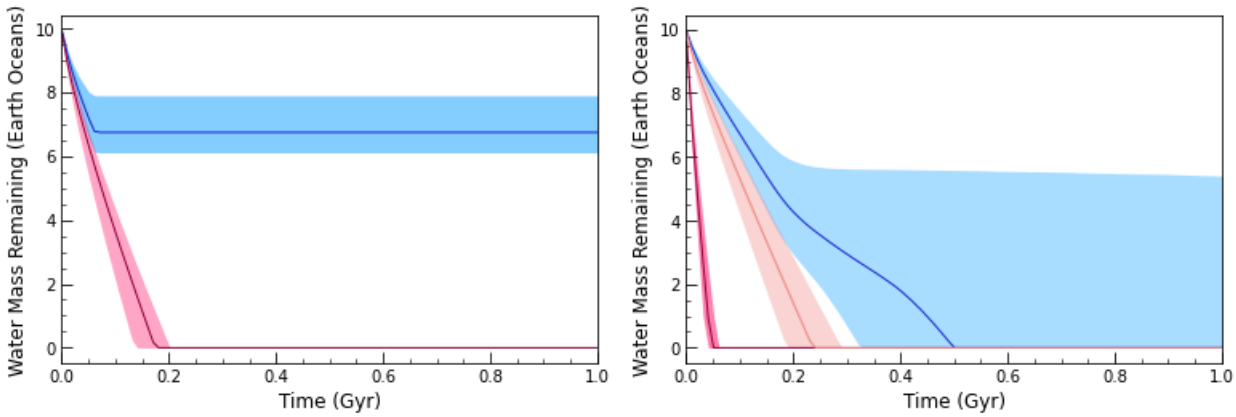

Figure 3.6: Water loss over time for all planets in the TOI 256 (left panel) and 700 (right panel) systems. On the left, TOI 256 b is shown in blue and 256 c is shown in red. On the right, planet 700 b is shown in red, 700 c is shown in peach, and 700 d is shown in blue. As water loss in the model is tied to the runaway greenhouse phase, models that deviate from this phase early lose less water. As shown in other figures and in the model description, this strongly correlates with the predicted mass of the planet.

without desiccated values to examine the distribution of remaining water mass should the planet retain water. This resulted in $4.69^{+2.53}_{-2.72}$ Earth oceans remaining. We find that for TOI 700d and smaller planets, this non-zero value is more appropriate to consider as the prospective mass of desiccated cases is inconsistent with reasonable density for a rocky planet.

3.4.2.2 TOI 256 b

All simulations of TOI 256 b returned non-desiccated models with $6.73^{+1.14}_{-0.62}$ Earth oceans of water remaining. As this planet has a mass consistent with a rocky planet (Dittmann et al. (2017); Lillo-Box et al. (2020)), these simulations indicate that TOI 256 b could likely have a large ocean covering most if not all of the surface as has been previously predicted (e.g., Lillo-Box et al. (2020)).

3.4.3 Discussion

As the model for water loss is an approximation and many other factors that influence the hydrodynamic outflow of a planet's hydrosphere have been neglected, the results of this study are no final judgement of a target's habitability. In addition, further and significant loss of water has been shown to occur in a nitrogen-poor Earth atmosphere following the early runaway greenhouse period (Wordsworth & Pierrehumbert (2013)) Figure Figure 3.6 clearly shows this as the models cease losing water the moment the early runaway greenhouse period ends.

To combat these factors, we made an effort to induce a more conservative modeling procedure by turning on efficient oxygen sinks, beginning the model at $t = 1Myr$, and removing any initial hydrogen envelope that might shield the water from XUV radiation.

Metric	Median	-1σ	$+1\sigma$
TOI 256 b			
Desiccation %	0%	···	···
Remaining Water Inventory (Earth Oceans)	6.733	0.622	1.138
Non-desiccated Inventory (Earth Oceans)	···	···	···
Final Static %	100%	···	···
Desiccation Rate (Earth Oceans/Gyr)	···	···	···
TOI 700 d			
Desiccation %	50.8%	···	···
Remaining Water Inventory (Earth Oceans)	0	0	5.811
Non-desiccated Inventory (Earth Oceans)	4.694	2.719	2.531
Final Static %	63.1%	···	···
Desiccation Rate (Earth Oceans/Gyr)	2.602	0.805	1.600

Table 3.5: Dessication Metrics

However, the results conveyed are likely accurate within a few factors and constitute a sufficiently robust prediction of water retention on the targets to inform followup observations which might shed further light on their specific scenarios.

3.4.3.1 Comparison With Initial Simulations

In Section subsection 3.2.1, we outlined preliminary simulations using *VPlanet* and a MCMC method using static distributions as opposed to simulations completed using the MCMC trace from directly fitting *TESS* data.

These initial simulations differ significantly in terms of desiccation rates compared to the new method outlined in this work. TOI 700 d increased in the number of desiccated models by around 20% whereas TOI 256 b decreased from around 15% to no desiccated models. These differences, and the discrepancies between the two targets is due to the new method detailed herein which more accurately treats the potential parameter distributions and inherently accounts for cross-correlations between parameters.

3.4.3.2 Mass Dependence for Rocky Bodies

Figure Figure 3.4 illustrates the dependance of water retention on the mass of the planet for TOI 700 d. At masses lower than the median predicted mass in log space, $1.4 M_{\oplus}$, the planet is certainly desiccated, but at masses indicating a terrestrial density, the planet only loses a maximum of 8 Earth oceans of water. As expected, more massive planets retain more water as their surface gravity is higher. The example of TOI 700 d clearly shows the necessity of thorough radial velocity measurements of smaller exoplanets as density, and thus mass, are such strong predictors of hydrosphere stability.

3.4.3.3 Density Dependence for Intermediate Bodies

Figure Figure 3.5 presents the desiccation of TOI 256 b against the predicted density used in the model. This is similar to the previous figure, but as this planet's radius is in the Fulton Gap (Fulton et al. (2017)), a naive mass approximation gives a relatively equal probability of it being rocky or gaseous. The density of Mars is used as a dividing line, highlighting the differences between these types of planets.

For rocky planets of this size, the curve follows much the same curve as TOI 700 d. As the density and thus the mass lowers, the planet is unable to retain the photodisassociated water and becomes desiccated. However, for gaseous planets, the amount of water retained increases with decreasing density for a portion of the distribution. This is due to the implied presence of an extended gaseous envelope that both protects the lower atmospheric water from disassociation and prevents Hydrogen and Oxygen from outflowing effectively. Similarly to the previous target, the case of TOI 256 b highlights the usefulness of radial velocity measurements in determining the potential habitability of an exoplanet.

3.4.3.4 Comparison of TOI 700 d to Other Studies

Suissa et al. (2020) explored 20 possible climate scenarios for TOI 700 d using the ExoCAM modeling package. Of these scenarios, the most likely ones given the work in our study are aqua planets in synchronous orbits. As we predict the loss of a significant amount of water, this correlates with the buildup of a relatively large amount of O2 on the planet's surface (Luger & Barnes (2014)). As these simulations do not include a photochemical model, they neglect this significant factor. Because of this, more simulations including

photochemical modeling must be conducted to predict the potential atmospheric states more accurately.

3.4.3.5 Future Observation Recommendations

Unfortunately, TOI 700 will not be observed by *JWST* in its Cycle 1 observations, potentially due to its small size and thus signal-to-noise ratio. Hopefully, the potential existence of a fourth planet in the system will lead to TOI 700 becoming a higher priority system. Radial velocity measurements of TOI 700 d would greatly aid in further characterization of the planet and give a foundation for the planning of atmospheric observations with *JWST*.

Water on TOI 256 b was tentatively discovered using the *Hubble Space Telescope's* WFC3 (Edwards et al. (2020)). This, along with radial velocity observations using ESPRESSO (Lillo-Box et al. (2020)) strongly implies the existence of a large surface ocean on the planet which is consistent with our findings that TOI 256 b should lose little, if any, of its primordial and accumulated water. Observations of TOI 256 b in Cycle 1 of *JWST* are aimed at confidently identifying water and other volatiles present in the atmosphere of the planet.

3.5 Conclusions

We have analyzed two high priority *TESS* planets, TOIs 256 b and 700 d, for their potential to retain a stable hydrosphere using a new, flexible method that incorporates observational data as opposed to other methods which use assumed parameter distributions. Preserving the correlations inherent in data-fitting procedures, such as between the fitted radius and mass predictions, is an important step in assessing the habitability of exoplanets and deciding which, if any, future observations are needed for further refinement.

We applied the method to two highly prioritized TESS-observed planets, TOIs 256 b (LHS 1140 b) and 700 d and assessed the likelihood that they retain stable hydrospheres to the present day through several metrics. Even with conservative initial water inventories, both planets retain water in a significant number of modeled cases (100% and 49% respectively). In addition, both planets are highly likely to retain a significant amount of water if they are predominately rocky.

Further observations of both planets are upcoming priorities, with TOI 256 b to be observed by the recently launched and commissioned *JWST* in its first Cycle. The characterization of this planet's atmosphere will enable more precise simulations of other planets in the future, refining procedures for identifying and prioritizing potentially habitable planets.

Though TOI 700 d is not a target for *JWST's* Cycle 1, it remains a tantalizing target for radial velocity observations as well as more precise photochemical modeling. The difficulty of atmospheric observations of this planet is a concern. However, the potential for discovering a habitable Earthlike planet is undeniable.

This material is based upon work supported by the National Aeronautics and Space Administration under a FINESST Award No. 80NSSC20K1395 issued through the Mission Directorate.

This research is supported by the Arkansas High Performance Computing Center, multiple National Science Foundation grants, and the Arkansas Economic Development Commission.

This chapter includes data collected by the TESS mission. Funding for the TESS mission is provided by the NASA's Science Mission Directorate.

This research has made use of the Exoplanet Follow-up Observation Program website, which is operated by the California Institute of Technology, under contract with the National Aeronautics and Space Administration under the Exoplanet Exploration Program.

This publication makes use of data products from the Two Micron All Sky Survey, which is a joint project of the University of Massachusetts and the Infrared Processing and Analysis Center/California Institute of Technology, funded by the National Aeronautics and Space Administration and the National Science Foundation.

This work has made use of data from the European Space Agency (ESA) mission Gaia (https://www.cosmos.esa.int/gaia), processed by the Gaia Data Processing and Analysis Consortium (DPAC, https://www.cosmos.esa.int/web/gaia/dpac/consortium). Funding for the DPAC has been provided by national institutions, in particular the institutions participating in the Gaia Multilateral Agreement.

4 Probabilistic Climate Simulations of TOI 700 d Using ROCKE-3D: Fractional Habitability and Aridity

4.1 Introduction

The presence of stable, liquid water at the surface of a planet is one of the most essential ingredients for life as we know it. Indeed, most studies of exoplanet habitability have tied the definition of habitability to the existence of liquid water (e.g. Lammer et al. (2009), Kopparapu et al. (2014), Jansen et al. (2019)). In 3D General Circulation Models (GCMs) of exoplanets, clouds and aerosols as well as ocean convection have been shown to greatly affect the model climate (Yang et al. (2014); Wang et al. (2016); Way & Wang (2019); Del Genio et al. (2019a)). 1D models, by their nature, cannot simulate these physical mechanisms which can impact the spatial and temporal distribution of liquid surface water, thus affecting habitability.

The recent launch and commissioning of the James Webb Space Telescope (JWST) provides an exciting opportunity to study the atmospheres of the numerous exoplanets discovered orbiting bright stars, many discovered by NASA's Kepler/K2 and Transiting Exoplanet Survey Satellite (TESS) Missions. The role of GCMs in this investigation are two-fold: forward modeling based on existing data to predict observations and retrieval modeling to determine the properties of planets based on the new observations. The work discussed in this chapter falls under the former category, forward modeling of known exoplanets based on previous observations.

Due to the computational power and time required of GCMs, previous modeling has focused on smaller sets of parameters that are tangentially linked to observational data (e.g.Del Genio et al. (2019a), Turbet et al. (2016)). While this can still be a useful tool for exploring possible habitable scenarios for targets, accurate probabilistic modeling is necessary to not only observably differentiate between habitable and non-habitable cases, but also to estimate the likelihood that a planet is habitable before committing the limited time resources of powerful telescopes, such as JWST, to their observation.

To this end, I have devised a scheme to probabilistically investigate the habitability of terrestrial exoplanets using the GCM ROCKE-3D (Way et al., 2017). This scheme exploits the statistical nature of previously derived posterior traces for fitting TESS data tables 3.3 and 3.4 to create a statistical link between observational data and sophisticated 3D models of a target's atmosphere.

The ROCKE-3D model is limited to exploring the properties of temperate, terrestrial worlds. Thus, I have applied this method to TOI 700 d, the most Earth-like TESS planet examined by my previous methods. In order to quantify the habitability of this target, I adopt two metrics: fractional habitability (i.e. the fraction of the planet between $0°C - 100°C$) and aridity (i.e. the net supply of water to land). Both have been used previously with this model to examine the habitability of warm, Earth-like planets (Jansen et al. (2019), Del Genio et al. (2019b) respectively). I use these metrics and novel method to estimate the probability that TOI 700 d is suitable for life as we know it.

In Section 2 I describe the ROCKE-3D model, its strengths and weaknesses, and its relevance to this project. In Section 3, I discuss the methods used in this study. Section 4 outlines the setup method for each model simulation including assumptions held during

the modeling process. In Section 4, I present the results of this ongoing study to date and discuss those results in Section 5. A brief conclusion and discussion of future work on this study follows in Section 6.

4.2 Climate Model

Climate modeling began, in large part, to understand terrestrial climate and man-made climate change (e.g. Manabe & Strickler (1964); Hansen et al. (1981)). The first models used were 1D radiative-convective models that simulated vertical atmospheric heat and particle transport. Models of this kind have several distinct advantages, namely speed and precision in complex physical, chemical, and radiative processes. However, 1D models fail to account for inherently 3D processes such as clouds, latitudinal and longitudinal heat transport, and spatial distribution of habitable areas. Because of this, lower resolution 3D GCMs quickly replaced 1D models to properly model the terrestrial climate.

GCMs have been used to simulate other planets' climates since the first Mars model of Leovy & Mintz (1969). Since then, GCMs have simulated a broad range of planets from large, hot, Jupiter-sized exoplanets to small, cool, rocky planets. GCMs have become an invaluable tool in exoplanet habitability studies to assess the impact of physical processes that are unable to be modeled in 1D.

4.2.1 ROCKE-3D

The ROCKE-3D (Resolving Orbital and Climate Keys of Earth and Extraterrestrial Environments with Dynamics; Way et al. (2017)) model is a derivative of an Earth GCM, the NASA Goddard Institute for Space Sciences ModelE2 (Schmidt et al., 2014). ROCKE-3D is

developed in tandem with the the ModelE branch, allowing the model to benefit immediately from new understandings of Earth's climate processes that are also relevant to other planets. The current version of ROCKE-3D is referred to as Planet 1.0, though an updated Planet 2.0 version is expected to be completed and distributed soon.

ROCKE-3D has been used to simulate Venus (e.g. Way et al. (2016); Way et al. (2022)), Mars (e.g. Guzewich et al. (2021)), and habitable scenarios for Proxima Centauri b (Del Genio et al., 2019a) among many other studies of planetary climate dynamics. The studies introducing the habitability metrics used in this study (Jansen et al. (2019), Del Genio et al. (2019a)) also make use of ROCKE-3D.

4.2.1.1 Model Features

The fully coupled dynamic ocean model available in ROCKE-3D was used for this climate study with a 4° x 5° resolution and 13 ocean layers. This configuration more accurately describes interactive ocean heat transport effects than other configurations (e.g. limiting ocean dynamics to surface interactions). As it has been shown that dynamically interacting, coupled oceans can produce a more modulated planet temperature, especially on tidally-locked worlds (e.g. Hu & Yang (2014)), this configuration is vital to realistically assess the stability of liquid water in the model.

ROCKE-3D is coupled to the Suite of Community Radiative Transfer codes based on Edwards and Slingo (SOCRATES, Edwards & Slingo (1996); Edwards (1996)) available from the UK Met Office. SOCRATES is a two-stream radiative transfer code that uses the correlated-k method (Lacis & Oinas (1991); Goody et al. (1989)), to parameterize gas absorption. Line-by-line cross-sections are calculated using the HITRAN 2012 line list (Rothman

et al., 2013) and the k-coefficients are calculated for each gas and band, though the number of k-coefficients varies with the required accuracy (Amundsen et al., 2014).

Input files for SOCRATES must be recalculated for each star-atmosphere combination as the methods described above are dependent both on the spectral profile of the host star and the atmospheric constituents of the modeled planet. In addition, the wavebands used in the model are relatively broad and must be tuned to avoid errors related to fluctuations in the source function within a band, particularly in the near-IR. Spectral files for this project were requested and created by Dr. Eric Wolf at the University of Colorado Boulder. The configuration used in this study includes 21 shortwave and 12 longwave bands (Tables Table 4.1 & Table 4.2)

The model allows cloud fraction to change dynamically based on relative humidity and convective stability in the grid box. In addition, it simulates the subgrid convecting of moist air instead of prescribing a relative humidity. Only water subgrid convection and clouds are modeled in ROCKE-3D in the current version and some Earth-specific tuning lingers in this version of the model. This is not anticipated to affect the results of this study as the clouds are optically thick Elsaesser et al. (2017).

ROCKE-3D accumulates snow and ice on land, but does not include a dynamic land ice model between grid cells. Because of this, land ice cannot grow or shrink across grid area. Instead, ice and snow grow or shrink in thickness and runoff from ice is handled via a parameterized glacial melt at pre-prescribed areas set at model start based on geography. Sea ice, on the other hand, is handled dynamically. This is especuially important for tidally-locked exoplanet modeling as it can prevent "cold trapping" of water advected to the night side of the planet (Yang et al., 2014). Albedo for all ice and snow is handled dynamically and

Band	Lower Limit	Upper Limit
1	200	320
2	320	505
3	505	690
4	690	770
5	770	890
6	890	980
7	980	1040
8	1040	1100
9	1100	1160
10	1160	1240
11	1240	1340
12	1340	1420
13	1420	1520
14	1520	1620
15	1620	1800
16	1800	1960
17	1960	2380
18	2380	2950
19	2950	4100
20	4100	4500
21	4500	20000

Table 4.1: Shortwave Bands Used (nm)

Band	Lower Limit	Upper Limit
1	25.00	1000
2	18.18	25.00
3	16.95	18.18
4	13.33	16.94
5	12.50	13.33
6	10.10	12.50
7	8.93	10.10
8	8.13	8.93
9	7.52	8.13
10	6.66	7.52
11	4.95	6.66
12	3.33	4.95

Table 4.2: Longwave Bands Used (μm)

changes with the state of the ice/snow (e.g. accumulating, melting, age of accumulation).

Geography in the model is prescribed at model start and can include any configuration across the grid squares with the exception that the south pole must be a land square. Grid cells are defined as land, water, or a fraction of both for coastlines if needed. The default geography is the Earth's. Water movement across land and runoff is handled via an assigned runoff file that is taken as an input to the model. This must be re-calculated for different geographical configurations prior to model start. Lakes may be set to dynamically form in areas of low topography as well as grow and shrink with rainfall and runoff.

4.2.2 Model Limitations

ROCKE-3D has a few limitations that have been kept in mind for this study. Firstly, the model is restricted to a 4° x 5° horizontal resolution, 20 or 40 atmospheric layers, and 13 ocean layers when run with a fully coupled ocean model. This causes some issues with dynamical effects that occur wholly within those cells. The target's predicted rotation rate and surface pressure are relatively close to the Earth's (37 days and 1700 millibar respectively) and thus its Rossby radius of deformation, the typical length scale of mid-latitude pressure centers, is appropriately large at all latitudes and will not cause problems with this limitation.

The top of the atmosphere is set to 0.1 hPa (65 km for Earth); the stratosphere is described only with mixing ratios derived from lower levels. For this reason, the model does not handle atmospheric escape. Based on previous work in Chapter 2, atmospheric escape for TOI 700 d in the modern day is expected to be negligible, satisfying this requirement.

The model is also limited to shallow atmospheres (i.e. scale height is small compared

to the radius). This precludes the model from studying mini-Neptunes, larger rocky bodies, and planets with thick or extended atmospheres. As the radius obtained for TOI 700 d is near the Earth's size ($1.12R_{\oplus}$) and is expected to be terrestrial in nature (Gilbert et al., 2020), ROCKE-3D is a well-tested and appropriate model for a climate study. TOI 256 b, which was studied during the work described in Chapter 2, is larger ($1.65R_{\oplus}$) and is expected to have a thicker, water-rich, atmosphere (Lillo-Box et al. (2020); Edwards et al. (2020)), making ROCKE-3D inappropriate to use for a climate study of this target.

Chemistry in the model is limited to O_2-bearing atmospheres and is not meant for more exotic atmospheres, especially reduced atmospheres such as Titan and early Earth simulations. For the purposes of this study, I assume that the atmosphere is akin to Earth's, so this limitation is not relevant. However, as the atmospheric constituents of TOI 700 d are currently unconstrained, a more thorough look at potential atmospheres is warranted in the future, though this will require an update to the model's chemistry or the employment of a different model.

4.3 Study Methods

One of the biggest detractors of attempting a large-scale study with many GCM models is the computational time required. In order to make valid inferences about a model climate, it needs to be, at least somewhat, energy balanced with respect to the incoming radiation from the host star. Using the fully coupled dynamic ocean makes this process take thousands of model orbits as the ocean is a large thermal sink. To combat this, one model using previous literature values for the target's parameters (Table 4.3; reffered to as the "median model") is created initially and allowed to run until it has an average net energy

balance within $\pm 0.2 \frac{W}{m^2}$ of 0 over the last 100 orbits. Once the model reaches this equilibrium, the final state of the model is captured in a file to bootstrap a suite of models based on the TESS lightcurve fitting done previously.

This novel method theoretically allows subsequent models to come into equilibrium much faster as the median model state is much closer to the equilibrium state of these child models than the initial state of the median model. I show in Section 4 that this is indeed the case. In order to minimize computational time needed, subsequent models are ordered based on the relative distance of the relevant parameters to the median model according to:

$$\Sigma_{i=1}^{n} \left| \frac{x_i - x_{i,med}}{x_{i,med}} \right| \tag{4.1}$$

where x_i is a parameter and $x_{i,med}$ is the median value for the parameter. 20 initial models were selected (Table 4.4) for this initial study, though models for most posterior parameter sets will be attempted eventually. Exceptions to this are non-physical parameter sets (e.g. density that suggests a gas planet) and extremes that are unable to be modeled by ROCKE-3D (e.g. insolation significantly higher or lower than Earth's).

Parameter Inputs	
Parameter	Initial Value
$g(\frac{m}{s^2})$	13.075
$P_{surf}(mbar)$	1747
$R_p(R_\oplus)$	1.19
$T(days)$	37.426
$S(\frac{W}{m^2})$	1170.18
Initial Condition Files	
Type of Initial Condition	File Name
Atmospheric	AIC.RES_M20A.D771201_40L.nc
Ground	GIC.E046D3M20A.1DEC1955.ext_1.nc
Ocean (bathtub)	OIC4X5LD.Z12.gas1.CLEV94.DEC01_btub00.nc
Ocean Function Table	OFTABLE_NEW
Ocean Basins	KB4X513.OCN.gas1.nc
Land Topography	Z72X46N_gas.1_nocasp_btub005.nc
Ocean Topography	OZ72X46N_gas.1_nocasp_btub005.nc
Ocean Straits	OSTRAITS_72x46btub0.nml
River Directions	RD_modelE_M_btub004D.nc
River Outlet Names	RD_modelE_M.Names_btub0.txt
Surface Drag Coefficient	CD4X500S.ext.nc
Vegitation Fraction (no vegetation)	V72X46.1.cor2_no_crops02.ext.nc
Crops (no crops)	CROPS2007_72X46N.cor4_nocasp.nc
Soil	S4X50093SANDCLAY.ext.nc
Topographical Variation	ZVAR4X5.nc
Soil Carbon	soilcarb_top30cm_4x5.nc
Glacier Melt Parameterization	GLMELT_4X5.OCN_MWAY0.nc
Greenhouse Gas Table	GHG.MWAY201412B.txt

Table 4.3: Median Model Parameter and Relevant File Inputs. All initial condition files are packaged with the model or requested as needed from GISS.

4.4 Simulation Setup

A list of the initial input files for the median model is available in Table 4.3.

The physical and orbital parameters of interest to this study are: surface gravity, g, surface pressure, P_{surf}, planet radius, R_p, sidereal orbital period, T, and insolation, S. As the planet is assumed to be tidally-locked based on VPLanet simulations, the sidereal rotation period is set to the sidereal orbital period and obliquity is set to 0 for all simulations. In addition, eccentricity is set to 0 as a circular orbit was previously assumed to obtain the posterior trace.

Planet radius and period are outputs of the fitting procedure in Chapter 2. In order to calculate the remaining parameters, the planet mass, M_p, and host star radius, R_*, are also needed. The surface gravity is calculated with respect to Earth's:

$$g = \left(\frac{M_p}{M_\oplus}\right) * \left(\frac{R_\oplus}{R_p}\right)^2 * g_\oplus \tag{4.2}$$

where $g_\oplus = 9.880665 \frac{m}{s^2}$ is the surface gravity of Earth. Assuming that the atmospheric mean molecular weight and total atmospheric mass is the same as Earth, the surface pressure can be estimated as:

$$P_{surf} = \left(\frac{M_p}{M_\oplus}\right)^2 * \left(\frac{R_\oplus}{R_p}\right)^4 * P_{surf,\oplus} \tag{4.3}$$

where $P_{surf,\oplus} = 985$ mbar is the average surface pressure on Earth. For insolation, I first calculated the insolation for the median model relative to the Earth:

$$S = \left(\frac{R_*}{R_\odot}\right)^2 * \left(\frac{365.25 days}{T}\right)^{\frac{4}{3}} * S_\oplus \tag{4.4}$$

Parameter Inputs

Trace Number	$g(\frac{m}{s^2})$	$P_{surf}(mbar)$	$R_p(R_\oplus)$	$T(days)$	$S(\frac{W}{m^2})$
122	13.345	1796.732	0.99565	37.436	1274.173
479	12.901	1679.108	1.00592	37.449	1271.548
835	14.058	1993.984	0.98328	37.425	1195.187
3898	13.222	1763.727	0.99901	37.423	1194.445
4914	13.046	1717.258	1.00099	37.438	1269.931
7557	12.241	1511.811	1.01878	37.416	1249.057
8694	12.425	1694.353	1.01058	37.424	1218.552
9124	13.342	1795.866	1.00980	37.434	1158.225
9125	12.715	1631.243	1.00857	37.438	1142.388
10376	13.049	1717.926	0.99895	37.432	1234.029
10608	12.104	1478.052	1.01396	37.426	1168.114
11429	13.108	1733.639	0.99069	37.441	1187.929
12094	13.051	1718.391	0.99485	37.413	1242.511
13218	13.104	1772.741	1.00287	37.432	1286.567
14076	12.452	1564.394	1.01700	37.413	1246.191
15743	13.069	1723.248	1.01269	37.420	1222.348
15966	11.895	1427.658	1.02624	37.419	1223.459
17609	13.573	1858.804	0.99163	37.428	1244.833
18006	12.679	1622.056	1.01602	37.429	1235.262
18484	13.689	1890.523	0.98328	37.446	1170.836

Table 4.4: Subsequent Model Parameters.

where $R_\odot$ is the radius of the Sun, and $S_\oplus = 1367 \frac{W}{m^2}$ is insolation of Earth.

The atmosphere of the model is assumed to be like Earth's, though O_3 is not included in the model as its production rate in the model is heavily tuned to Earth values and is not necessarily valid in a different radiation environment. O_2 is included despite the fact that it should produce 0_3, though Dr. Michael Way has communicated that this does not affect the dynamics much at all.

Exoplanet geography and topography are entirely unconstrained and, as stated previously, changes in these can drastically impact the habitability of models. I decided to keep the default Earth geography and topography because the ocean transports heat to the night side of the planet well and this keeps the night side from freezing completely as in Yang et al. (2014). Though this choice is arbitrary, it is optimistic and designed to produce more habitable scenarios. The results of this study are dependent on this choice, though more studies specifically analyzing the effects of topography are needed to assess the true impact on the results. The only deviation from Earth topography is the inclusion of a "bathtub ocean" that is deep at the coastlines. This deep ocean basin prevents freezing of the coastline, which will crash the model. This initial state dynamically changes based on its prescribed physical and orbital parameters and its radiation environment.

ROCKE-3D has the capability to model the dynamical aspects of vegetation on climate, however, I chose not to include vegetation in this study as the status of complex life outside of Earth is unconfirmed. Furthermore, the scope of this study is focused on the potential for habitability, not the effects of life on the target's climate.

As TOI 700 d is presumed to be tidally-locked, the choice of the substellar point is important (e.g. Fujii et al. (2017), Kane et al. (2018)). For these simulations, the substellar

point is set to be in what would be the Pacific Ocean on Earth. The choice of a substellar point over an ocean leads to rapid evaporation of water, creating a blanketing cloud layer and modulating surface temperature. A substellar point over dry land, however, can cause the surface to become incredibly hot very quickly as in Kane et al. (2018). As the model's radiation tables are valid to around 400K, this could quickly crash the model. As with the choice of Earth geography and topography, this is a more optimistic choice that will lead to better heat distribution and, theoretically, more habitable area on the planet's surface.

4.5 Results

The median model came into equilibrium around 4500 orbits into the simulation, requiring 500 hours of wall-clock time. Subsequent models came into equilibrium as early as 500 subsequent orbits later, only requiring 55 hours of wall-clock time, almost an order of magnitude improvement in time requirements. As of the time of this dissertation submission, xx models have come into equilibrium (including the median model), yy models are still running, and zz models have failed (Table 4.5).

Model Name	Convergence Status	Fractional Habitabilty	Fractional Aridity	Fractional Aridity (Non-zero PET)
Median	Converged (5000 orbits)	0.5676515	0.5815223	0.30038238
122	Broken (model instability)	···	···	···
479	Broken (model instability)	···	···	···
835	Broken (frozen ocean)	···	···	···
3898	Broken (unknown)	···	···	···
4914	Broken (model instability)	···	···	···
7557	Unconverged (500 Orbits)	···	···	···
8694	Unconverged (500 Orbits)	···	···	···
9124	Converged (500 orbits)	0.58439124	0.13250056	0.22486138
9125	Broken (model instability)	···	···	···
10376	Broken (model instability)	···	···	···
10608	Converged (500 orbits)	0.55699444	0.54582256	0.26831523
11429	Broken (frozen ocean)	···	···	···
12094	Broken (model instability)	···	···	···
13218	Broken (model instability)	···	···	···
14076	Unconverged (500 Orbits)	···	···	···
15743	Broken (model instability)	···	···	···
15966	Unconverged (500 Orbits)	···	···	···
17609	Broken (model instability)	···	···	···
18006	Unconverged (500 Orbits)	···	···	···
18484	Unconverged (500 Orbits)	···	···	···

Table 4.5: Models' convergence status and results fro converged models. Only three models have converged so far including the median model. Models crashed due to instability will be reported to GISS and investigated for model improvements.

I calculate fractional habitability using the formulation from Jansen et al. (2019):

$$f_H(T_{rot}) = \frac{1}{A_{tot}} \sum_{i=1}^{n_\theta} \sum_{j=1}^{n_\phi} H(\theta, \phi, T_{rot}) A_{i,j} \tag{4.5}$$

where $H(\theta, \phi, T_{rot})$ is the habitability per grid cell averaged over at least one orbital period and diurnal cycle, T_{rot}, for a specific orbital period. The definition of $H(\theta, \phi, T_{rot})$ is taken from Spiegel et al. (2009):

$$H(\theta, \phi, T_{rot}) = \left\{ \begin{array}{ll} 1, & if 0 \leq t(\theta, \phi, T_{rot})[^\circ C] \leq 100 \\ 0, & else \end{array} \right\} \tag{4.6}$$

Thus, fractional habitability is essentially a measure of the area fraction of the planet that is within the temperature range for liquid water. It is noted that for substantially higher or lower pressures, this value will not be accurate as the critical points of water fluctuate. However, for the pressure ranges I simulate, this fluctuation is negligible.

Aridity is taken to be:

$$A = \frac{Pr}{(Pr + PET)} \tag{4.7}$$

as in Del Genio et al. (2019b) and (Scheff & Frierson, 2015). This value is taken from values averaged over the same time scale as fractional habitability, but the dependencies are absent from the equation above for simplicity. Pr is the orbit averaged precipitation in a grid cell in $\frac{mm}{day}$ and PET is potential evapotranspiration, or the amount of evaporation that would occur if a sufficient water source were available. This essentially measures the net ratio of water incident on the surface of that grid cell. The inclusion of Pr in the denominator

bounds the metric between 0 and 1.

For the value of PET, I use a version of the Penman-Monteith equation which is the standard reference equation for the American Society of Civil Engineers and the Food and Agriculture Organization (ASCE/FAO; Allan et al. (1998)):

$$PET = \frac{0.408\Delta(R_n - G) + \gamma \frac{900}{T_a+273} u_2(e_s - e_a)}{\Delta + \gamma(1 + 0.34u_2)} \tag{4.8}$$

The numerical values in this equation come from agricultural applications and assume aerodynamic resistance and bulk surface resistance based on parameter values for an assumed reference crop type. Higher values of PET would occur for bare soil as in this model, but Scheff & Frierson (2014) show that this has a relatively small effect on the primary climate drivers of PET. From the above equation, Δ is the slope of the saturation vapor pressure curve. This can be estimated using:

$$\Delta = \frac{4080[0.6108 * exp(\frac{17.27T_{mean}}{T_{mean}+237.3})]}{(T_{mean} + 237.3)^2} \tag{4.9}$$

where T_{mean} is the average of the minimum and maximum diurnal temperatures in $^\circ C$ for the grid cell. R_n is the net surface radiation, taken from the model in units of Wm^{-2} and converted into units of $MJm^{-2}day^{-1}$. G is the topsoil heat flux density, or the net heat into the surface soil, also taken from the model with the same unit conversion. γ is the psychometric constant which is defined as:

$$\gamma = \frac{C_p P}{\epsilon L_v} \tag{4.10}$$

or the ratio of specific heat (C_p) of moist air at a constant pressure (P) in kPa to latent heat (L_v) of vaporization of water weighted by the ratio of molecular weight of water vapor to dry air (ϵ). I adopt the values of the three constants, C_p, L_v, and ϵ from Allan et al. (1998) which yeilds:

$$\gamma = 0.665x10^{-3}P \tag{4.11}$$

At the pressures and temperatures in the model, these constants vary negligibly from the assumed amounts. T_a is the temperature at 2m above the surface. This is taken to be surface air temperature from the model as this is where the surface atmospheric grid box is situated. u_2 is the wind speed in the same vertical grid box. Finally, the vapor pressure deficit, $(e_s - e_a)$ is calculated from the actual vapor pressure (e_a) and average saturation vapor pressure (e_s). The actual vapor pressure can be calculated in terms of the saturation vapor pressure and mean relative humidity (RH_m):

$$e_a = \frac{RH_m}{100} e_s \tag{4.12}$$

where the average saturation vapor pressure can be found in terms of minimum and maximum temperature (T_{min}, T_{max}):

$$e_s = \frac{0.6108}{2}\left[e^{\frac{17.27*T_{max}}{Tmax+237.3}} + e^{\frac{17.27*T_{min}}{T_{min}+237.3}}\right] \tag{4.13}$$

I adopt the convention of Del Genio et al. (2019b) and Scheff & Frierson (2015) for two extreme hydroclimactic regimes: $A > 0.39$ indicates a humid climate and $A < 0.17$

indicates an arid climate. $A > 0.39$ is indicative of tropical rain forest environments and $A < 0.17$ indicates most deserts on Earth.

For each converged model, I present a chart showing the net radiation balance for the last 100 years. This average must be within ± 0.2 of 0 for the model to be in equilibrium. In addition, I show a similar chart for yearly fractional habitability and fractional aridity which is calculated similarly with the exception that only land grids are counted. Finally, I show an image of the global map for average aridity and temperature for the last 100 model years. The final metrics for fractional habitability and aridity are given for the average of the same time frame.

4.5.1 Median Model's Results

The median model displays remarkably temperate average surface temperatures(Figure 4.2), especially around the terminator. This strongly indicates a habitable scenario for over half of the planet and results in a fractional habitability of 0.568. The fractional aridity metric initially derived is 0.582, however, the value for PET becomes negative for most of the night side because of a supersaturated atmosphere (Figure 4.4). This leads to a value for aridity that is higher than 1, so I set all cells with this problem to have an aridity of 0. This method yielded 0.300 fractional land aridity, indicating a relatively humid climate.

This modeling appears to avoid the worst fate of slowly rotating models in DDel Genio et al. (2019b) where the entire planet is stuck in the supersaturated state of the night side. This is likely due to the more extreme water cycle driven by a large ocean under the substellar point and the lack od a diurnal cycle. More modeling is needed to determine the effect of different substellar points on the habitability metrics.

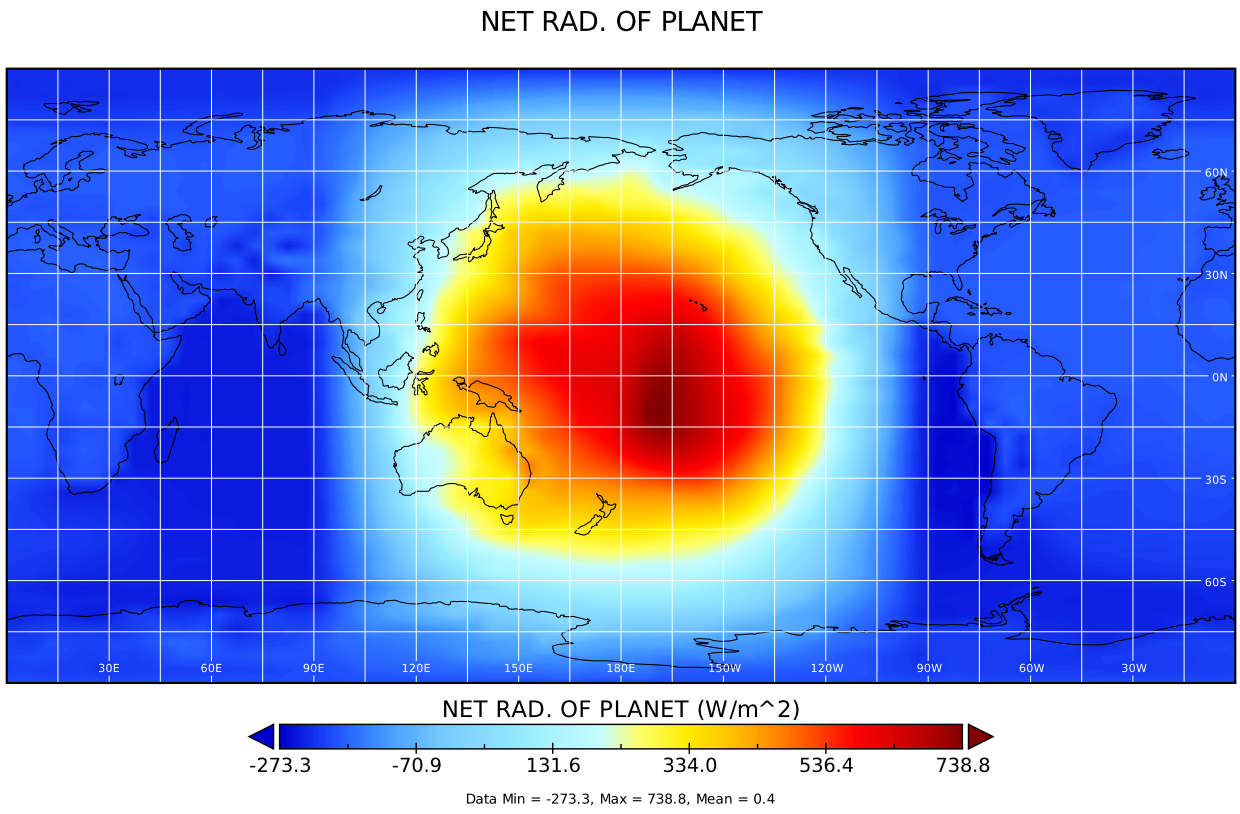

Figure 4.1: Average Net radiation for the median model of TOI 700 d. The substellar point is clearly visible in the middle of the "Pacific Ocean." Figure made using Panoply.

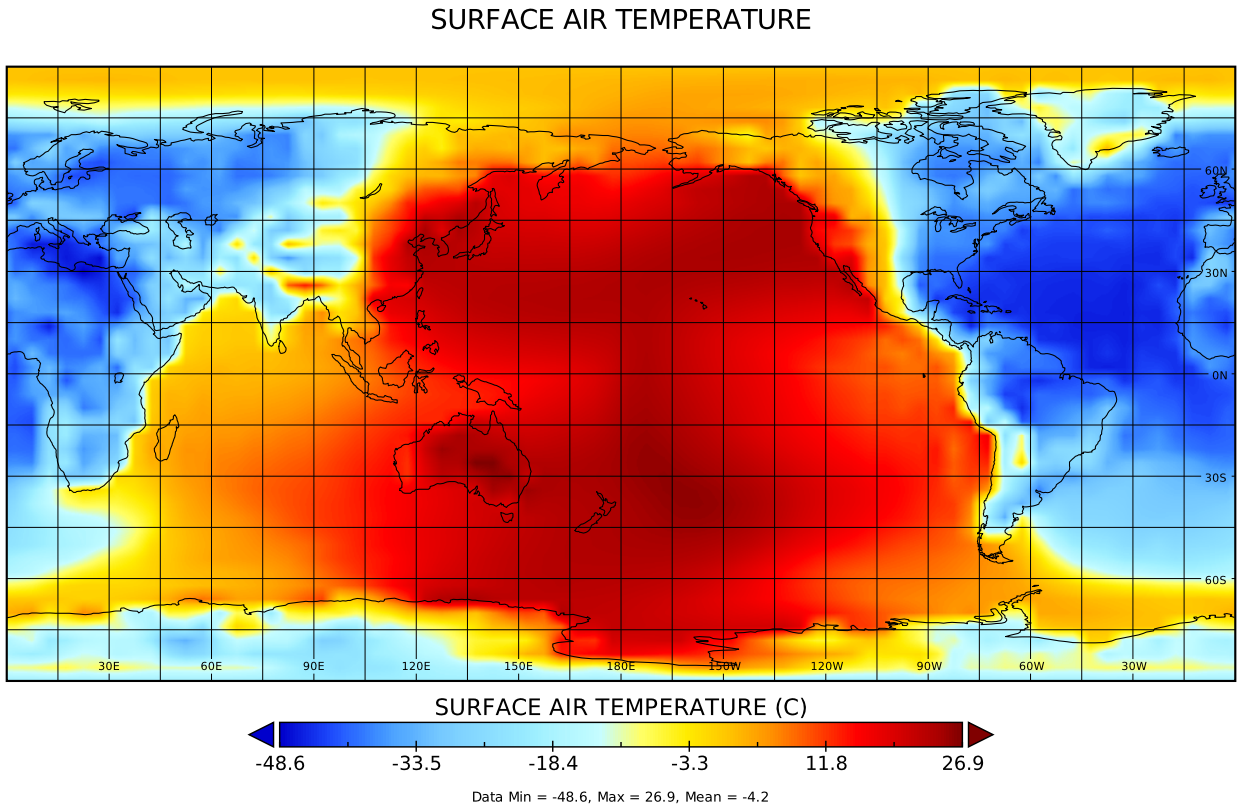

Figure 4.2: Average surface temperature for the median model of TOI 700 d. Most of the planet appears to be capable of sustaining liquid water. Figure made using Panoply.

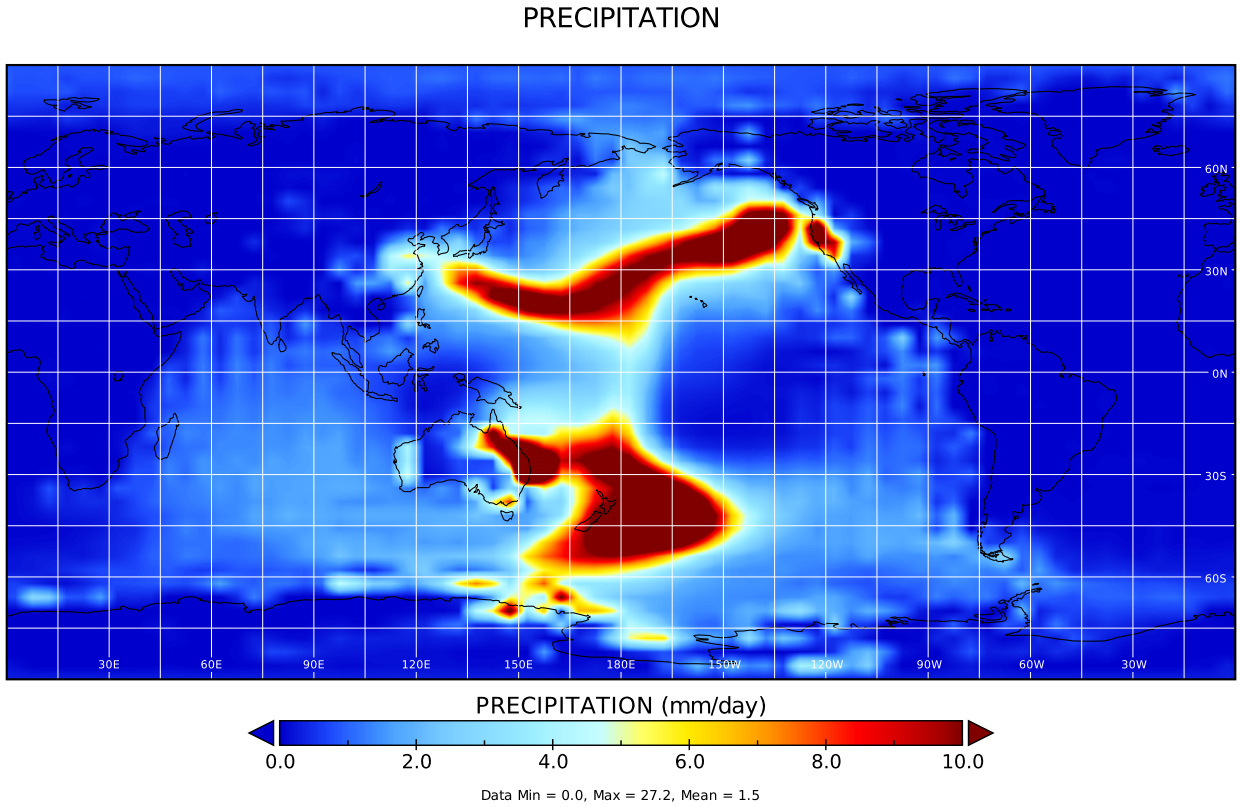

Figure 4.3: Average precipitation for the median model of TOI 700 d. Heaviest precipitation is seen to mainly occur on coasts 'facing' the substellar point on the day side of the planet. For reference, the annual averaged global rainfall of the Earth is $2.7\frac{mm}{day}$ Figure made using Panoply.

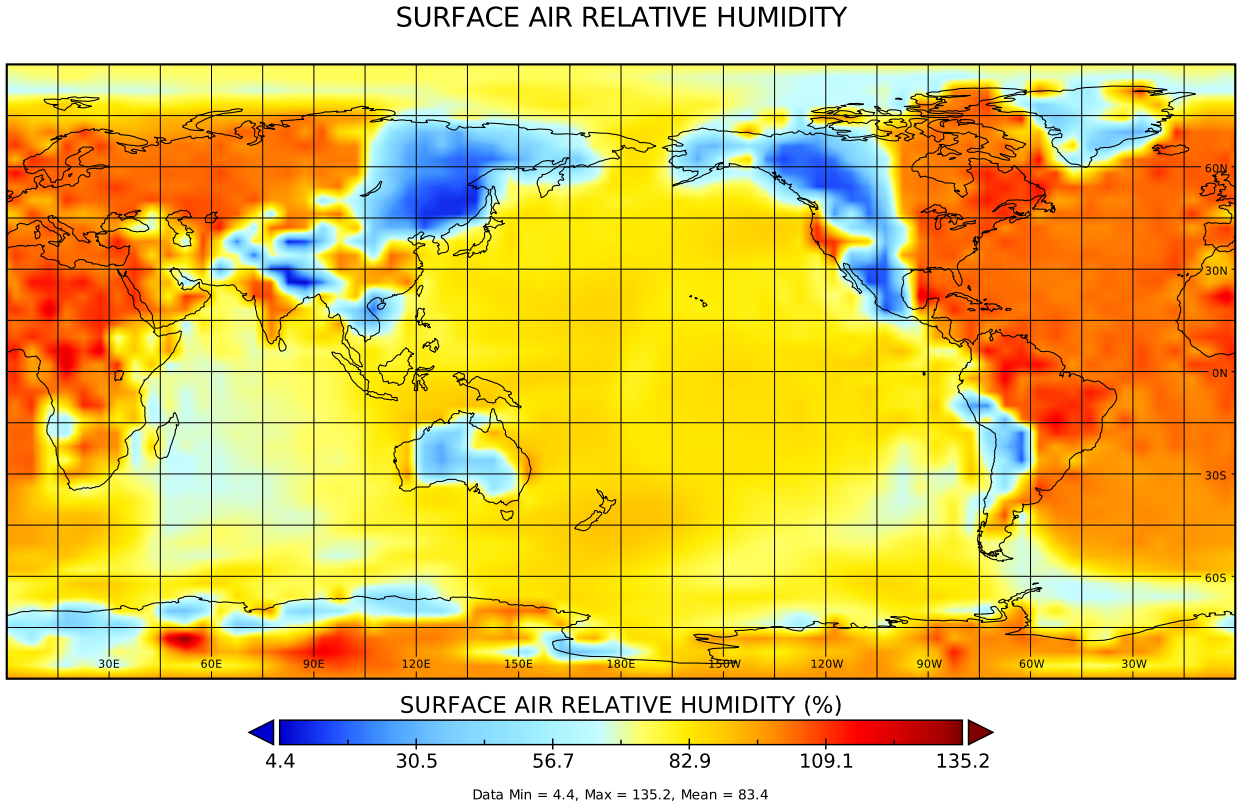

Figure 4.4: Average surface relative humidity for the median model of TOI 700 d. The night side's relative humidity rises above 100% as it becomes supersaturated from the warm, moist air coming from the day side. Figure made using Panoply.

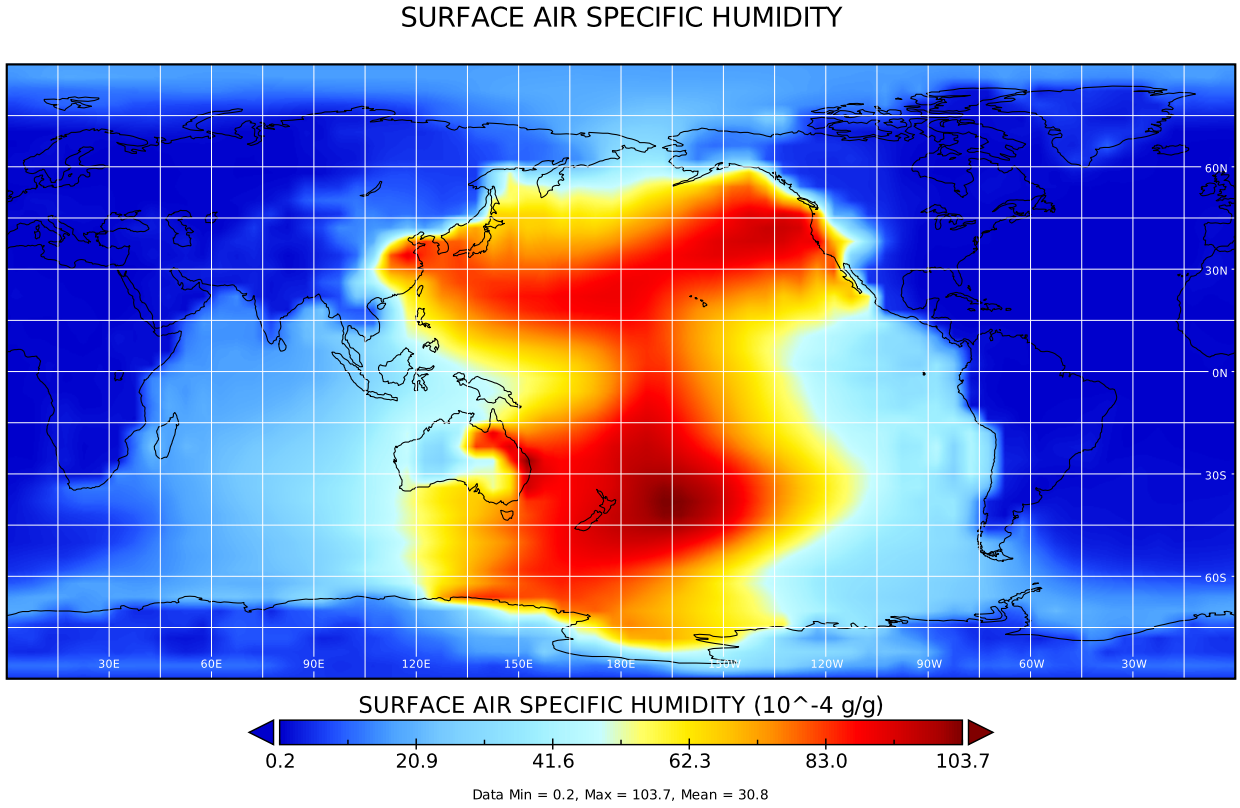

Figure 4.5: Average surface specific humidity. The night side clearly has little water to precipitate, making it highly arid despite the aridity metric described in this work. Figure made using Panoply.

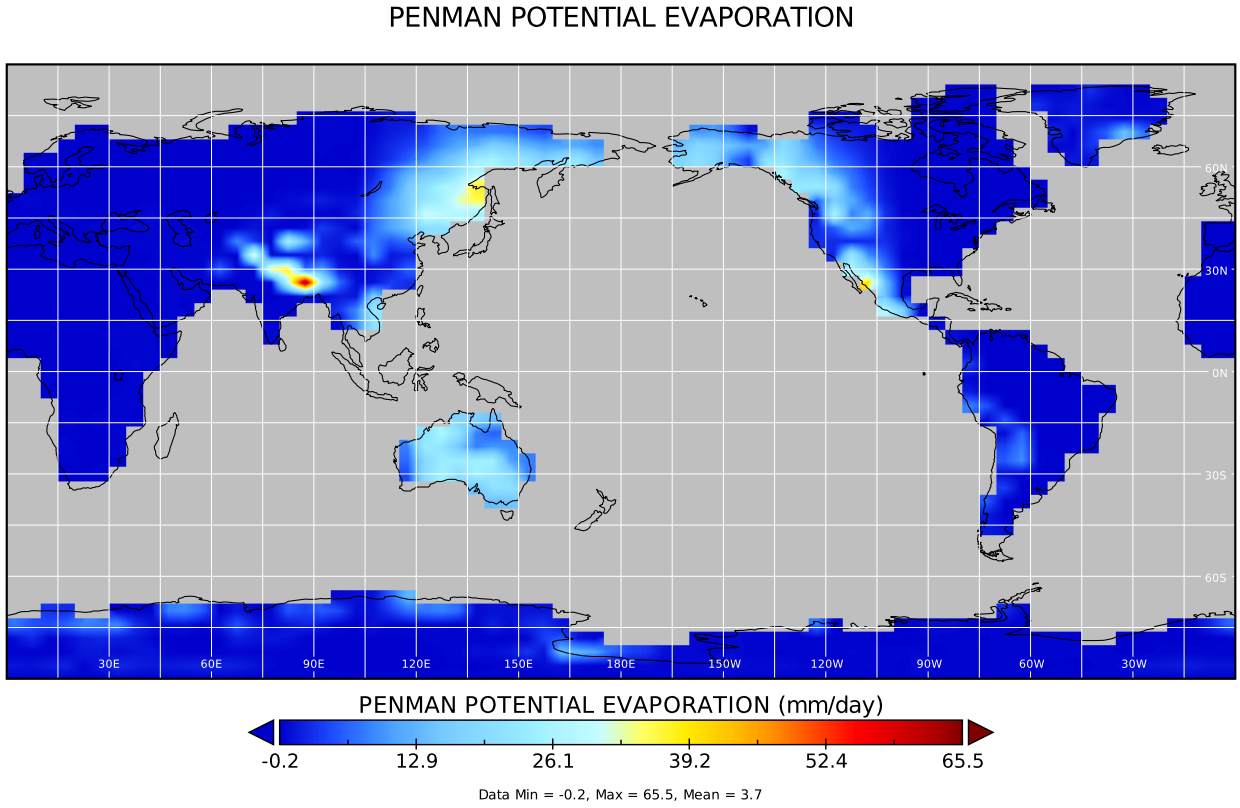

Figure 4.6: Pennman potential evaporation for the median model of TOI 700 d. The model tracks a version of the metric described in this work. The value becomes negative when relative humidity rises above 100%. Figure made using Panoply.

4.5.2 Converged Models' Results

Subsequent modeling has so far been in-line with the median model. The two models that have converged from the initial set show similar fractional habitabilities of 0.584 and 0.557 and fractional land aridity of 0.225 and 0.268.

Interestingly, the 9124 model increased in fractional land aridity when negative PET values were removed. This is due to some grid cells having negative PET values that exceeded precipitation. Physically, this corresponds to land that is soaking up all available water and releasing none of it, corresponding with a 0 value for aridity as no water will be stabily available at the surface.

4.6 Discussion

Based on preliminary results of converged models, the simulations show that TOI 700 d is potentially habitable given the assumptions in this study. The surface temperature lends itself particularly to the definition of habitability adopted in this work (i.e. stable liquid surface water). Areas that experience precipitation on the day side and along the terminator could support life as we know it.

It is interesting to note that, though most of the surface is relatively humid, most places do not experience much precipitation (Figure 4.3). This is due to low specific humidity (Figure 4.5), which is only high on the day side of the planet and at the terminator. These results indicate that more of the day side of TOI 700 d may be habitable given an Earth-like atmosphere and surface ocean. These areas are a temperate environment that should experience moderate to extreme rainfall. For reference, the U.S. experiences an average of

around $2\frac{mm}{day}$ of rainfall (NCEI.Monitoring.Info@noaa.gov, 2020).

4.6.1 Unconverged Models

Most models that have crashed have done so from instabilities in the model's ocean dynamics code. These crash reports, along with all relevant information, will be forwarded to GISS to aid in model development. If these models are outside of the boundary conditions of the model, it will be noted in Table 4.5 when this is confirmed. Otherwise, when updated ocean dynamics are available, the crashed models will be restarted and allowed to run until crashed or converged.

Models that have not crashed and are still in disequilibrium will be continued. Even if all crashed models are unable to be salvaged, roughly half of the models so far appear to be stable. If this ratio holds, this should result more than enough simulations to draw robust conclusions at the time when all models are finished. At this point, results will be submitted for publication in a peer-reviewed journal.

4.6.2 Method Analysis

The novel, probabilistic approach applied to 3D GCMs appears to be working with great success. Several subsequent models bootstrapped from the median have converged nearly an order of magnitude faster than the initial model, allowing for more in-depth statistical modeling whit this complex model.

The simulations completed in this work are limited in scope to relatively Earth-like climates and topography. More modeling of this kind is needed to assess other potential climates on this world. Additionally, high precision transit spectroscopy and radial velocity

measurements are needed to further constrain the atmosphere and bulk properties of TOI 700 d respectively. Combined, models and observation could confirm the first habitable planet besides Earth.

4.7 Conclusion

In this chapter, I have described a novel scheme to probabilistically investigate the habitability of terrestrial exoplanets using the GCM ROCKE-3D. Using previously derived posterior traces from fitting TESS data, I created a statistical link between observational data and sophisticated 3D models of a target's climate.

By way of the fractional habitability and aritity metrics, I have shown how to determine potential habitable climates for TOI 700 d as well as how habitable those scenarios are. The initial simulations done with this setup reveal a potentially habitable climate on TOI 700 d with over half the surface being habitable temperature-wise (fractional habitability $= 0.568$). Additionally, the models do not appear to be arid (fractional land aridity $= 0.3$) meaning that hypothetical surface life would be able to readily access a robust water cycle similar in some places to a tropical rainforest on Earth.

Subsequent simulations display similar, encouraging, results. Once further simulations finish coming into equilibrium, these results, along with the background in this chapter and further statistical analysis, will be submitted to a peer-reviewed journal for publication.

Further avenues of study based on this research could include exploring other potential climates such as a Mars or Titan analogue, though these would require a new version of ROCKE-3D or a different model altogether. In addition, more research is needed to explore the impact of efficient ocean heat transportation on these metrics. A final example could be

an exploration of the effects biological life on the climate in an attempt to find biosignatures for future detection.

This material is based upon work supported by the National Aeronautics and Space Administration under a FINESST Award No. 80NSSC20K1395 issued through the Mission Directorate.

This research is supported by the Arkansas High Performance Computing Center, multiple National Science Foundation grants, and the Arkansas Economic Development Commission.

This chapter includes data collected by the TESS mission. Funding for the TESS mission is provided by the NASA's Science Mission Directorate.

This research has made use of the Exoplanet Follow-up Observation Program website, which is operated by the California Institute of Technology, under contract with the National Aeronautics and Space Administration under the Exoplanet Exploration Program.

This publication makes use of data products from the Two Micron All Sky Survey, which is a joint project of the University of Massachusetts and the Infrared Processing and Analysis Center/California Institute of Technology, funded by the National Aeronautics and Space Administration and the National Science Foundation.

This work has made use of data from the European Space Agency (ESA) mission Gaia (https://www.cosmos.esa.int/gaia), processed by the Gaia Data Processing and Analysis Consortium (DPAC, https://www.cosmos.esa.int/web/gaia/dpac/consortium). Funding for the DPAC has been provided by national institutions, in particular the institutions participating in the Gaia Multilateral Agreement.

5 Conclusion

The search for extraterrestrial life has so far yielded no conclusive results. As the detection capabilities of telescopes improve, however, it is only a matter of time until we answer the question: are we alone? Until then, it is important to prioritize the limited time we have to use the powerful observatories at our disposal and focus on those exoplanets that are most hospitable to life as we know it. To this end, I have created and applied a novel method to probabilistically analyze the potential habitability of exoplanets using TESS data and a suite of models.

In Chapter 1, I outlined the WGSCM, a quick and flexible approach to prioritizing targets. This method was then applied to the TESS CTL and the most Earth-like planets, TOIs 256 b and 203 b, were identified. Though the metrics used have limitations and are not necessarily an accurate correlation with habitability, the method has proven itself to be a capable first-look prioritization scheme for ordering targets for further review.

In Chapter 2, I described a novel, data-based method to analyze the primordial water loss of TESS targets using the posterior distributions of a MCMC fit to their lightcurves. The method was applied to the most Earth-like candidates identified through the work in Chapter 1 as well as the most Earth-like TESS planet, TOI 700 d. TOI 203 b was found to likely be devoid of water in initial testing, though TOI 256 b and 700 d were found to retain water in 100% and 49% of modeled cases respectively. In addition, both targets are highly likely to retain a significant amount of water if they are of terrestrial density, which is expected.

Finally, in Chapter 3, I applied this same scheme to a 3D GCM, ROCKE-3D, for TOI 700 d. Simulations were run assuming an Earth-analogue with the observable orbital and physical parameters of the target. Preliminary results show that TOI 700 d has a strong potential for being habitable given the assumptions of an Earth-like atmosphere, Earth topography, and a large substellar ocean. In addition, preliminary analysis of the probabilistic scheme indicate that its application to ROCKE-3D is a success; subsequent models bootstrapped from a median model converge up to an order of magnitude faster. Climate simulations for TOI 700 d are still ongoing and a publication will be prepared to share the results once modeling has concluded.

Bibliography

Alibert, Y. 2014, A&A, 561, A41, doi: 10.1051/0004-6361/201322293

Allan, R., Pereira, L., & Smith, M. 1998, Crop evapotranspiration-Guidelines for computing crop water requirements-FAO Irrigation and drainage paper 56, Vol. 56

Amundsen, D. S., Baraffe, I., Tremblin, P., et al. 2014, A&A, 564, A59, doi: 10.1051/0004-6361/201323169

Armstrong, D. J., Pugh, C. E., Broomhall, A. M., et al. 2016, MNRAS, 455, 3110, doi: 10.1093/mnras/stv2419

Armstrong, J. C., Barnes, R., Domagal-Goldman, S., et al. 2014, Astrobiology, 14, 277, doi: 10.1089/ast.2013.1129

Astropy Collaboration, Price-Whelan, A. M., Sipőcz, B. M., et al. 2018, AJ, 156, 123, doi: 10.3847/1538-3881/aabc4f

Baraffe, I., Homeier, D., Allard, F., & Chabrier, G. 2015, A&A, 577, A42, doi: 10.1051/0004-6361/201425481

Barnes, R., Deitrick, R., Luger, R., et al. 2016, arXiv e-prints, arXiv:1608.06919. https://arxiv.org/abs/1608.06919

Barnes, R., Luger, R., Deitrick, R., et al. 2020, PASP, 132, 024502, doi: 10.1088/1538-3873/ab3ce8

Becker, J., Gallo, E., Hodges-Kluck, E., Adams, F. C., & Barnes, R. 2020, The Astronomical Journal, 159, 275, doi: 10.3847/1538-3881/ab8fb0

Benedict, G. F., Henry, T. J., Franz, O. G., et al. 2016, The Astronomical Journal, 152, 141, doi: 10.3847/0004-6256/152/5/141

Berta-Thompson, Z. K., Irwin, J., Charbonneau, D., et al. 2015, Nature, 527, 204, doi: 10.1038/nature15762

Bloom, S. 1981, Marine Ecology Progress Series, 5, 125, doi: 10.3354/meps005125

Bolmont, E., Selsis, F., Owen, J. E., et al. 2016, Monthly Notices of the Royal Astronomical Society, 464, 3728, doi: 10.1093/mnras/stw2578

Bonney, P., & Kennefick, J. 2022, , 3, 202, doi: 10.3847/PSJ/ac8669

Boyajian, T. S., von Braun, K., van Belle, G., et al. 2012, ApJ, 757, 112, doi: 10.1088/0004-637X/757/2/112

Bray, J. R., & Curtis, J. T. 1957, Ecological Monographs, 27, 326. http://www.jstor.org/stable/1942268

Chambers, J. E. 2004, Earth and Planetary Science Letters, 223, 241, doi: 10.1016/j.epsl.2004.04.031

Chassefière, E. 1996, Icarus, 124, 537, doi: https://doi.org/10.1006/icar.1996.0229

Chassefière, E., Wieler, R., Marty, B., & Leblanc, F. 2012, Planetary and Space Science, 63-64, 15, doi: 10.1016/j.pss.2011.04.007

Crossfield, I. J. M., & Kreidberg, L. 2017, AJ, 154, 261, doi: 10.3847/1538-3881/aa9279

Del Genio, A. D., Way, M. J., Amundsen, D. S., et al. 2019a, Astrobiology, 19, 99, doi: 10.1089/ast.2017.1760

Del Genio, A. D., Way, M. J., Kiang, N. Y., et al. 2019b, ApJ, 887, 197, doi: 10.3847/1538-4357/ab57fd

Dittmann, J., Irwin, J., Charbonneau, D., et al. 2017, Nature, 544, 333, doi: 10.1038/nature22055

Dodd, M., Papineau, D., Grenne, T., et al. 2017, Nature, 543, 60, doi: 10.1038/nature21377

Edwards, B., Changeat, Q., Mori, M., et al. 2020, The Astronomical Journal, 161, 44, doi: 10.3847/1538-3881/abc6a5

Edwards, J. M. 1996, Journal of Atmospheric Sciences, 53, 1921, doi: 10.1175/1520-0469(1996)053<1921:ECOIFA>2.0.CO;2

Edwards, J. M., & Slingo, A. 1996, Quarterly Journal of the Royal Meteorological Society, 122, 689, doi: 10.1002/qj.49712253107

Elsaesser, G. S., Del Genio, A. D., Jiang, J. H., & van Lier-Walqui, M. 2017, Journal of Climate, 30, 317, doi: 10.1175/JCLI-D-16-0346.1

Erkaev, N. V., Kulikov, Y. N., Lammer, H., et al. 2007, A&A, 472, 329, doi: 10.1051/0004-6361:20066929

ExoFOP. 2019, Exoplanet Follow-up Observing Program - TESS, IPAC, doi: 10.26134/EXOFOP3

Fleming, D. P., Barnes, R., Luger, R., & VanderPlas, J. T. 2020, The Astrophysical Journal, 891, 155, doi: 10.3847/1538-4357/ab77ad

Foreman-Mackey, D., Agol, E., Angus, R., & Ambikasaran, S. 2017, The Astronomical Journal, 154, doi: 10.3847/1538-3881/aa9332

Foreman-Mackey, D., Hogg, D. W., Lang, D., & Goodman, J. 2013, PASP, 125, 306, doi: 10.1086/670067

Foreman-Mackey, D., Luger, R., Agol, E., et al. 2021, The Journal of Open Source Software, 6, 3285, doi: 10.21105/joss.03285

Fujii, Y., Del Genio, A. D., & Amundsen, D. S. 2017, ApJ, 848, 100, doi: 10.3847/1538-4357/aa8955

Fulton, B. J., Petigura, E. A., Howard, A. W., et al. 2017, AJ, 154, 109, doi: 10.3847/1538-3881/aa80eb

Gaia Collaboration, Prusti, T., de Bruijne, J. H. J., et al. 2016, A&A, 595, A1, doi: 10.1051/0004-6361/201629272

Gaia Collaboration, Brown, A. G. A., Vallenari, A., et al. 2018, A&A, 616, A1, doi: 10.1051/0004-6361/201833051

Gelman, A., & Rubin, D. B. 1992, Statistical Science, 7, 457, doi: 10.1214/ss/1177011136

Gilbert, E. A., Barclay, T., Schlieder, J. E., et al. 2020, AJ, 160, 116, doi: 10.3847/1538-3881/aba4b2

Goody, R., West, R., Chen, L., & Crisp, D. 1989, J. Quant. Spec. Radiat. Transf., 42, 539, doi: 10.1016/0022-4073(89)90044-7

Guzewich, S. D., Way, M. J., Aleinov, I., et al. 2021, Journal of Geophysical Research (Planets), 126, e06825, doi: 10.1029/2021JE006825

Hansen, J., Johnson, D., Lacis, A., et al. 1981, Science, 213, 957, doi: 10.1126/science.213.4511.957

Hoffman, M. D., & Gelman, A. 2011, arXiv e-prints, arXiv:1111.4246. https://arxiv.org/abs/1111.4246

Hu, Y., & Yang, J. 2014, Proceedings of the National Academy of Science, 111, 629, doi: 10.1073/pnas.1315215111

Hunten, D. M., Pepin, R. O., & Walker, J. C. G. 1987, Icarus, 69, 532, doi: 10.1016/0019-1035(87)90022-4

Jansen, T., Scharf, C., Way, M., & Del Genio, A. 2019, ApJ, 875, 79, doi: 10.3847/1538-4357/ab113d

Jenkins, J. M., Twicken, J. D., McCauliff, S., et al. 2016, in Software and Cyberinfrastructure for Astronomy IV, ed. G. Chiozzi & J. C. Guzman, Vol. 9913, International Society for Optics and Photonics (SPIE), 1232 – 1251, doi: 10.1117/12.2233418

Kane, S. R., Ceja, A. Y., Way, M. J., & Quintana, E. V. 2018, ApJ, 869, 46, doi: 10.3847/1538-4357/aaec68

Kanodia, S., Wolfgang, A., Stefansson, G. K., Ning, B., & Mahadevan, S. 2019, ApJ, 882, 38, doi: 10.3847/1538-4357/ab334c

Kasting, J. F. 1988, Icarus, 74, 472, doi: 10.1016/0019-1035(88)90116-9

Kipping, D. M. 2013a, Monthly Notices of the Royal Astronomical Society, 435, 2152, doi: 10.1093/mnras/stt1435

—. 2013b, Monthly Notices of the Royal Astronomical Society: Letters, 434, L51, doi: 10.1093/mnrasl/slt075

Kleine, T., Touboul, M., Bourdon, B., et al. 2009, Geochim. Cosmochim. Acta, 73, 5150, doi: 10.1016/j.gca.2008.11.047

Kopparapu, R. K., Ramirez, R. M., SchottelKotte, J., et al. 2014, ApJ, 787, L29, doi: 10.1088/2041-8205/787/2/L29

Kopparapu, R. K., Ramirez, R., Kasting, J. F., et al. 2013, ApJ, 765, 131, doi: 10.1088/0004-637X/765/2/131

Kostov, V. B., Schlieder, J. E., Barclay, T., et al. 2019, AJ, 158, 32, doi: 10.3847/1538-3881/ab2459

Kumar, R., Carroll, C., Hartikainen, A., & Martin, O. 2019, The Journal of Open Source Software, 4, 1143, doi: 10.21105/joss.01143

Lacis, A. A., & Oinas, V. 1991, J. Geophys. Res., 96, 9027, doi: 10.1029/90JD01945

Lammer, H., Erkaev, N. V., Odert, P., et al. 2013, MNRAS, 430, 1247, doi: 10.1093/mnras/sts705

Lammer, H., Bredehöft, J. H., Coustenis, A., et al. 2009, A&A Rev., 17, 181, doi: 10.1007/s00159-009-0019-z

Leconte, J., Forget, F., Charnay, B., Wordsworth, R., & Pottier, A. 2013, Nature, 504, 268, doi: 10.1038/nature12827

Leconte, J., Wu, H., Menou, K., & Murray, N. 2015, Science, 347, 632, doi: 10.1126/science.1258686

Lehmer, O., & Catling, D. 2017, The Astrophysical Journal, 845, 130, doi: 10.3847/1538-4357/aa8137

Leovy, C., & Mintz, Y. 1969, Journal of Atmospheric Sciences, 26, 1167, doi: 10.1175/1520-0469(1969)026<1167:NSOTAC>2.0.CO;2

Lightkurve Collaboration, Cardoso, J. V. d. M., Hedges, C., et al. 2018, Lightkurve: Kepler and TESS time series analysis in Python. http://ascl.net/1812.013

Lillo-Box, J., Figueira, P., Leleu, A., et al. 2020, A&A, 642, A121, doi: 10.1051/0004-6361/202038922

Lopez, E. D., Fortney, J. J., & Miller, N. 2012, ApJ, 761, 59, doi: 10.1088/0004-637X/761/1/59

Lopez, E. D., & Rice, K. 2018, MNRAS, 479, 5303, doi: 10.1093/mnras/sty1707

Luger, R., Agol, E., Foreman-Mackey, D., et al. 2019, AJ, 157, 64, doi: 10.3847/1538-3881/aae8e5

Luger, R., & Barnes, R. 2014, Astrobiology, 15, doi: 10.1089/ast.2014.1231

Luger, R., Barnes, R., Lopez, E., et al. 2015, Astrobiology, 15, 57, doi: 10.1089/ast.2014.1215

Luri, X., Brown, A. G. A., Sarro, L. M., et al. 2018, A&A, 616, A9, doi: 10.1051/0004-6361/201832964

Manabe, S., & Strickler, R. F. 1964, Journal of Atmospheric Sciences, 21, 361, doi: 10.1175/1520-0469(1964)021<0361:TEOTAW>2.0.CO;2

Mann, A. W., Feiden, G. A., Gaidos, E., Boyajian, T., & von Braun, K. 2015, ApJ, 804, 64, doi: 10.1088/0004-637X/804/1/64

Mann, A. W., Dupuy, T., Kraus, A. L., et al. 2019, ApJ, 871, 63, doi: 10.3847/1538-4357/aaf3bc

Mayor, M., & Queloz, D. 1995, Nature, 378, 355, doi: 10.1038/378355a0

Ment, K., Dittmann, J. A., Astudillo-Defru, N., et al. 2019, The Astronomical Journal, 157, 32, doi: 10.3847/1538-3881/aaf1b1

Morbidelli, A., Chambers, J., Lunine, J. I., et al. 2000, Meteoritics & Planetary Science, 35, 1309, doi: https://doi.org/10.1111/j.1945-5100.2000.tb01518.x

NCEI.Monitoring.Info@noaa.gov. 2020, Annual 2020 National Climate Report. https://www.ncei.noaa.gov/access/monitoring/monthly-report/national/202013

Ning, B., Wolfgang, A., & Ghosh, S. 2018, ApJ, 869, 5, doi: 10.3847/1538-4357/aaeb31

Owen, J. E., & Wu, Y. 2013, ApJ, 775, 105, doi: 10.1088/0004-637X/775/2/105

—. 2017, ApJ, 847, 29, doi: 10.3847/1538-4357/aa890a

O'Malley-James, J. T., & Kaltenegger, L. 2017, Monthly Notices of the Royal Astronomical Society: Letters, 469, L26, doi: 10.1093/mnrasl/slx047

Parker, E. N. 1964, ApJ, 139, 93, doi: 10.1086/147741

Pecaut, M. J., & Mamajek, E. E. 2013, ApJS, 208, 9, doi: 10.1088/0067-0049/208/1/9

Ramirez, R. M., & Kaltenegger, L. 2018, ApJ, 858, 72, doi: 10.3847/1538-4357/aab8fa

Raymond, S. N., Kokubo, E., Morbidelli, A., Morishima, R., & Walsh, K. J. 2014, in Protostars and Planets VI, ed. H. Beuther, R. S. Klessen, C. P. Dullemond, & T. Henning, 595, doi: 10.2458/azu_uapress_9780816531240-ch026

Raymond, S. N., Quinn, T., & Lunine, J. I. 2006, Icarus, 183, 265, doi: 10.1016/j.icarus.2006.03.011

Reid, I.N. & Hawley, S. 2005, New Light on Dark Stars (Springer)

Ribas, I., Guinan, E. F., Güdel, M., & Audard, M. 2005, ApJ, 622, 680, doi: 10.1086/427977

Rothman, L. S., Gordon, I. E., Babikov, Y., et al. 2013, J. Quant. Spec. Radiat. Transf., 130, 4, doi: 10.1016/j.jqsrt.2013.07.002

Salvatier, J., Wiecki, T. V., & Fonnesbeck, C. 2016, PeerJ Computer Science, 2, e55, doi: 10.7717/peerj-cs.55

Scalo, J., Kaltenegger, L., Segura, A., et al. 2007, Astrobiology, 7, 85, doi: 10.1089/ast.2006.0125

Scheff, J., & Frierson, D. M. W. 2014, Journal of Climate, 27, 1539, doi: 10.1175/JCLI-D-13-00233.1

—. 2015, Journal of Climate, 28, 5583, doi: 10.1175/JCLI-D-14-00480.1

Schmidt, G. A., Kelley, M., Nazarenko, L., et al. 2014, Journal of Advances in Modeling Earth Systems, 6, 141, doi: 10.1002/2013MS000265

Schulze-Makuch, D., Méndez, A., Fairén, A., et al. 2011, Astrobiology, 11, 1041, doi: 10.1089/ast.2010.0592

Skrutskie, M. F., Cutri, R. M., Stiening, R., et al. 2006, AJ, 131, 1163, doi: 10.1086/498708

Sotin, C., Grasset, O., & Mocquet, A. 2007, Icarus, 191, 337, doi: https://doi.org/10.1016/j.icarus.2007.04.006

Spiegel, D. S., Menou, K., & Scharf, C. A. 2009, ApJ, 691, 596, doi: 10.1088/0004-637X/691/1/596

Stassun, K. G., Oelkers, R. J., Pepper, J., et al. 2018, AJ, 156, 102, doi: 10.3847/1538-3881/aad050

Strom, K. M., Strom, S. E., Edwards, S., Cabrit, S., & Skrutskie, M. F. 1989, AJ, 97, 1451, doi: 10.1086/115085

Suissa, G., Wolf, E. T., Kopparapu, R. k., et al. 2020, The Astronomical Journal, 160, 118, doi: 10.3847/1538-3881/aba4b4

The Theano Development Team, Al-Rfou, R., Alain, G., et al. 2016, arXiv e-prints, arXiv:1605.02688. https://arxiv.org/abs/1605.02688

Tsiaras, A., Waldmann, I. P., Tinetti, G., Tennyson, J., & Yurchenko, S. N. 2019, Nature Astronomy, 3, 1086, doi: 10.1038/s41550-019-0878-9

Turbet, M., Leconte, J., Selsis, F., et al. 2016, A&A, 596, A112, doi: 10.1051/0004-6361/201629577

Walter, F. M., Brown, A., Mathieu, R. D., Myers, P. C., & Vrba, F. J. 1988, AJ, 96, 297, doi: 10.1086/114809

Wang, Y., Liu, Y., Tian, F., et al. 2016, ApJ, 823, L20, doi: 10.3847/2041-8205/823/1/L20

Watson, A. J., Donahue, T. M., & Walker, J. C. G. 1981, Icarus, 48, 150, doi: 10.1016/0019-1035(81)90101-9

Way, M. J., Del Genio, A. D., Kiang, N. Y., et al. 2016, Geophys. Res. Lett., 43, 8376, doi: 10.1002/2016GL069790

Way, M. J., Ernst, R. E., & Scargle, J. D. 2022, , 3, 92, doi: 10.3847/PSJ/ac6033

Way, M. J., & Wang, J. 2019, Venus Topography and Boundary Conditions in 3D General Circulation Modeling, ed. H. Hargitai (Cham: Springer International Publishing), 325–335, doi: 10.1007/978-3-319-62849-3_19

Way, M. J., Aleinov, I., Amundsen, D. S., et al. 2017, ApJS, 231, 12, doi: 10.3847/1538-4365/aa7a06

Wordsworth, R. D., & Pierrehumbert, R. T. 2013, ApJ, 778, 154, doi: 10.1088/0004-637X/778/2/154

Yang, J., Liu, Y., Hu, Y., & Abbot, D. S. 2014, ApJ, 796, L22, doi: 10.1088/2041-8205/796/2/L22

Zahnle, K. J., & Kasting, J. F. 1986, Icarus, 68, 462, doi: https://doi.org/10.1016/0019-1035(86)90051-5